A Vlasov–Fokker–Planck code for high energy density physics

M. Tzoufras [a,b,*], A.R. Bell [a,b], P.A. Norreys [b], F.S. Tsung [c]

[a] Department of Physics, University of Oxford, Clarendon Laboratory, Parks Road, Oxford OX1 3PU, UK
[b] Central Laser Facility, STFC Rutherford Appleton Laboratory, Chilton, Didcot OX11 0QX, UK
[c] Department of Physics and Astronomy, University of California, Los Angeles, CA 90095, USA

ABSTRACT

OSHUN is a parallel relativistic 2D3P Vlasov–Fokker–Planck code, developed primarily to study electron transport and instabilities pertaining to laser-produced—including laser-fusion—plasmas. It incorporates a spherical harmonic expansion of the electron distribution function, where the number of terms is an input parameter that determines the angular resolution in momentum-space. The algorithm employs the full 3D electromagnetic fields and a rigorous linearized Fokker–Planck collision operator. The numerical scheme conserves energy and number density. This enables simulations for plasmas with temperatures from MeV down to a few eV and densities from less than critical to more than solid. Kinetic phenomena as well as electron transport physics can be recovered accurately and efficiently.

© 2011 Elsevier Inc. All rights reserved.

1. Introduction

1.1. The Vlasov–Fokker–Planck description of plasmas

Strong electromagnetic fields, steep temperature and pressure gradients, and rapid changes in boundary conditions are common in plasma physics and can be described using the Vlasov–Fokker–Planck equation [11,15,44,38]. This equation is valid whenever the collisions between plasma particles can be considered elastic Markovian and their effect can be calculated by linear addition of binary collision events for distances up to a Debye length $\lambda_D = \sqrt{k_B T/(4\pi n e^2)}$ [42]. These conditions are usually met, if the number of particles in a Debye sphere is large, $N_D = 4\pi\lambda_D^3/3 \gg 1$. Many types of plasmas fall in this category, including astrophysical, laser-produced and fusion plasmas. Thus, solving the VFP equation is of central importance in high energy density physics.

In Inertial Confinement Fusion [28], numerical solutions to the VFP equation can aid the design of shock ignition [7,35,37,39] and fast ignition [45,33,23,25,24] targets, by providing insight into fundamental physical processes, such as electron transport and resistive collimation. While addressing these issues is the main focus of the code presented here, the same technique can be straightforwardly adapted to model many other problems in plasma physics.

1.2. Motivation: the challenge of modeling fast ignition and shock ignition

In ICF a capsule of hydrogen isotopes (DT) implodes under ablation pressure and the isotopes fuse, releasing energy. Shock ignition and fast ignition have been proposed in order to increase the energy gain by an order of magnitude without

* Corresponding author at: Department of Physics, University of Oxford, Clarendon Laboratory, Parks Road, Oxford OX1 3PU, UK.
  E-mail address: m.tzoufras1@physics.ox.ac.uk (M. Tzoufras).

major modifications to conventional ICF designs. For example (a) a joint European project (HiPER) is being planned [19], which will take advantage of the low ignition threshold associated with fast ignition (or shock ignition) to drastically shrink the size and cost of the drive laser system; (b) a Japanese project (FIREX) has been launched to achieve fast ignition [2]; and (c) near term fast/shock ignition experiments are being considered at the Lawrence Livermore National Laboratory to demonstrate order-of-magnitude higher gains.

Fast ignition relies on the electrons at the surface of the compressed pellet to absorb the energy of an ultra-intense laser pulse and efficiently transfer that energy to the core. For shock ignition, the hot electrons generated near the critical surface due to a spike in the drive laser pulse, must distribute the energy around the compressed pellet so as to launch a spherically convergent shock. In both cases hot electrons travel from the hot near-critical plasma corona to the cooler dense collisional plasma. The transport of this large population of hot electrons through and around the dense plasma is associated with the generation of strong electromagnetic fields—and a number of instabilities—which in turn are determined by the plasma heat conduction. In this regime classical heat conduction does not apply (see [4,29]) and a fully kinetic description of the electron distribution must be considered.

The VFP equation allows for kinetic modeling of the entire electron population and can be readily applied to plasmas with densities from subcritical to more than solid and temperatures as high as MeV and as low as a few eV. In conjunction with the standard expressions for the Coulomb logarithm [20], this equation provides a reliable description of the large volume of plasma between the laser-plasma interface, where $N_D \gtrsim 10^5$, and the ultra-high density region. Using the same approach to model regions where $N_D \lesssim 1$ presents no numerical difficulties, provided a minimum positive value is used for the Coulomb logarithm. However, for non-ideal plasmas the applicability of the Fokker–Planck collision operator itself is questionable. Warm Dense Matter (WDM) physics must be incorporated to simulate such plasmas.

1.3. Approaches to modeling high energy density physics

1.3.1. Particle-In-Cell

Particle-In-Cell models work at the most elementary level by calculating the interaction between individual simulation particles and the associated electromagnetic fields. In order to capture this microscopic behavior a mesh that resolves the Debye length (λ_D) is required. In ICF, where temperatures in the plasma corona are in the keV to MeV range, λ_D can be much longer than the laser wavelength. Deeper in the target, where the temperature is lower the density higher and collisions dominate, λ_D decreases rapidly, for example in a 300 eV plasma with density $10^{23}/cc$ it is about 4 Å. Under such conditions it is nearly impossible to resolve the Debye length for a system with any physically relevant size, even in 2D. This limits the utility of traditional PIC simulations in this regime.

Sentoku and Kemp [40] and Chrisman et al. [13] proposed using reduced-PIC codes, which under-resolve the Debye length and employ weighted particles, to simulate collective effects with wavelength longer than λ_D in dense low-temperature plasmas. In this scheme the collisionally dominated microphysics is modelled with Monte Carlo statistical techniques [34,40]. This approach substantially reduces the computational requirements compared to standard PIC codes and has been used for large fast ignition simulations.

1.3.2. Hybrid Particle-In-Cell

Traditional hybrid codes speed up the calculation by splitting the electrons into two populations, fast and thermal, but this distinction is not always consistent with the physics. Moreover, because the fluid/thermal population is just that (fluid), it does not capture intricate structures in the distribution function, which are prevalent in fast ignition and shock ignition.

An exciting recent development in this area is a new type of hybrid code, recently proposed by Cohen et al. [14], which uses a Particle-In-Cell description of the plasma in the entire simulation domain and applies Ohm's law to determine the effect of the cold background electrons on the fields. Thus, a fully kinetic approach is used, and there is no sharp boundary between the strictly hybrid and strictly kinetic treatment. This promises to drastically relax the computational constraints for simulating plasmas with ultra-high density, thereby making 2D full-target fast ignition simulations conceivable.

1.3.3. Vlasov–Fokker–Planck

The VFP description is a fundamentally different approach to treating a system of particles compared to the Particle-In-Cell method. The latter employs a collection of finite-size particles to describe the plasma, whereas the former uses a distribution function and operators on that function to account for the effects of fields and advection and for individual particle interactions such as collisions. The main difficulty in solving the VFP equation numerically comes from the multidimensional nature of the electron distribution function, since even a modest number of cells per dimension can lead to a prohibitively large grid. This is in contrast to PIC codes, which use particles to dynamically sample the phase-space.

VFP codes were pioneered by Bell et al. [4] and Matte and Virmont [31] to investigate the effect of sharp temperature gradients on heat conduction. Their results established the importance of non-local transport for plasmas irradiated by intense lasers. In order to study electron transport over long time-scales, Kingham and Bell [22] developed an implicit nonrelativistic 2D VFP code. The first order terms of the cartesian tensor expansion of the distribution function (the diffusive approximation) were incorporated in this code, the displacement current was neglected, and the electric (magnetic) field was considered in (out of) the simulation plane. This approach was extended by Thomas et al. [46] who included
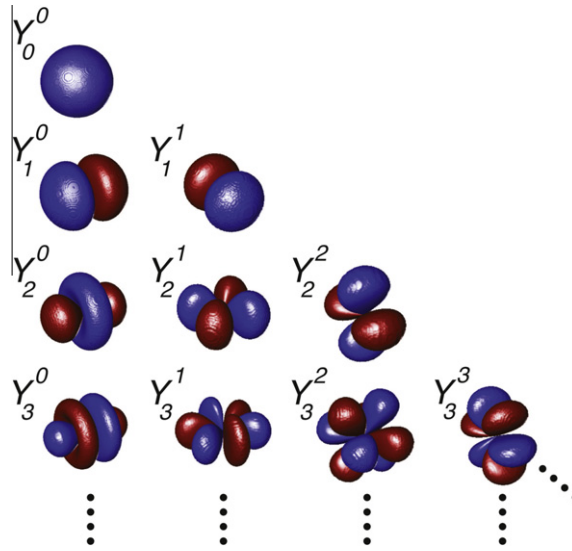
Fig. 1. Iso-surfaces of the first 10 spherical harmonics $Y_\ell^m, 0 \leqslant m \leqslant \ell \leqslant 3$ multiplied by e^{-p^2} (where p is the euclidian distance from the origin). The larger the indices ℓ, m are the more directional/anisotropic the harmonic Y_ℓ^m.

the second order terms, i.e. anisotropic pressure, in the cartesian tensor expansion. An alternative method by Sherlock [41], considered spherical coordinates in momentum-space without employing the expansion to cartesian tensors or spherical harmonics.

Recently, Duclous et al. [17] developed a nonrelativistic 2D3V Vlasov–Fokker–Planck–Landau code in cartesian geometry with the electric (magnetic) field in (out of) the plane, which can treat an arbitrary degree of anisotropy and may be used to model instabilities as well as electron transport. This approach is important for the validation of other methods relying on more assumptions, but its applicability is limited by the vast amount of computer memory required to model five dimensions in phase-space.

1.3.4. VFP with the full spherical harmonic expansion of the distribution function

In their classic paper, Rosenbluth et al. [38] used direction cosines (Legendre polynomials) to represent a cylindrically symmetric distribution in momentum-space. For asymmetric distribution functions the corresponding expressions involve the spherical harmonics (or cartesian tensors) and were discussed in detail by Shkarofsky et al. [42]. Accordingly, the distribution function is described by the complex amplitudes of the expansion.

Each spherical harmonic is discretized with a cartesian mesh in configuration-space and a 1D mesh for the magnitude of momentum $p \equiv |\boldsymbol{p}| = \sqrt{p_x^2 + p_y^2 + p_z^2}$. Its angular shape in momentum-space is characterized by two indices, ℓ and m, where large ℓ, m correspond to highly directional and anisotropic harmonics. The first 10 spherical harmonics with $0 \leqslant m \leqslant \ell \leqslant 3$, multiplied by a shape factor e^{-p^2}, are shown in Fig. 1. The main advantage of this approach is that angular scattering due to electron–ion collisions tends to isotropize the electron distribution by rapidly damping the high-order harmonics. It is therefore possible to capture most of the key physics using only a few terms in the expansion—depending on the degree of anisotropy and the collisionality of the plasma—and significantly reduce the problem size compared to a VFP code in cartesian geometry. Other advantages of this expansion include: that it allows one to resolve the magnitude of momentum much more finely than the angle, that it makes it easier to stretch the momentum-space, and that it facilitates the implementation of collisions between electrons. On the other hand, its main vulnerability, the singularity at the center of the coordinate system, $p = 0$, can be effectively addressed in the numerical scheme. The formulation of this approach was presented by Bell et al. [5] and it has been implemented in the VFP code OSHUN described in this article.

In shock ignition the electron temperatures in the plasma corona are typically up to 10 keV, and if LPI-generated hot electrons are considered, up to 100 keV. Shock ignition is therefore an excellent candidate for a VFP code that utilizes the expansion to spherical harmonics, because the plasma is collisional enough to be accurately modeled with a limited number of harmonics. On the other hand, in fast ignition the laser-heated electrons reach temperatures of several MeV and are almost collisionless. Consequently it may be necessary to use a PIC code for the coronal plasma and couple it to a VFP code, or to model electron heating with a PIC code and use the resulting distribution function as input for a VFP code. The VFP code can also be used to study the basic problem of transport of hot electrons in the presence of transverse resistivity gradients and the collisional current-filamentation instability. Both of these effects must be well-understood to assess the feasibility of the fast ignition concept.

2. Vlasov code

2.1. Theoretical model

2.1.1. Spherical harmonics

The spherical harmonics $Y_\ell^m(\theta, \varphi)$ are orthonormal functions of the colatitude θ ($0 \leqslant \theta < \pi$) and longitude/azimuth φ ($0 \leqslant \varphi < 2\pi$) and appear in problems that exhibit a significant degree of spherical symmetry. They are expressed as the product of the associated Legendre polynomials $P_\ell^m(\cos\theta)$ (including the Condon–Shortley phase) and the exponential function $e^{im\varphi}$:

$$Y_\ell^m(\theta, \varphi) = \sqrt{\frac{2\ell+1}{4\pi}\frac{(\ell-m)!}{(\ell+m)!}}P_\ell^m(\cos\theta)e^{im\varphi}, \quad -\ell \leqslant m \leqslant \ell. \tag{1}$$

A complex square-integrable function F can be expanded as $F = \sum_{\ell=0}^{\infty}\sum_{m=-\ell}^{\ell}F_\ell^m(p)Y_\ell^m(\theta, \varphi)$, where (p, θ, φ) are the spherical coordinates with p the euclidean distance from the origin. For a real function f a basis of real spherical (surface) harmonics $Y_{\ell ms}$ can be derived from Y_ℓ^m using $\begin{pmatrix} Y_{\ell m0} \\ Y_{\ell m1} \end{pmatrix} = \frac{1}{\sqrt{2}}\begin{pmatrix} 1 & (-1)^m \\ -i & i(-1)^m \end{pmatrix}\begin{pmatrix} Y_\ell^{|m|} \\ Y_\ell^{-|m|} \end{pmatrix}$. Invoking the property $P_\ell^{-m}(x) = (-1)^m\frac{(\ell-m)!}{(\ell+m)!}P_\ell^m(x)$ it can be shown that the surface harmonics are independent of the sign of m and can be written as functions of $|m|$ or $m \geqslant 0$:

$$Y_{\ell ms}(\theta, \varphi) = \sqrt{\frac{2\ell+1}{4\pi}\frac{(\ell-m)!}{(\ell+m)!}}P_\ell^m(\cos\theta) \times \begin{cases} [\delta_{0s}\cos(m\varphi) + \delta_{1s}\sin(m\varphi)]/\sqrt{2}, & m > 0, \\ \delta_{0s}\cos(m\varphi) & m = 0, \end{cases} \tag{2}$$

where δ_{ij} is the Kronecker delta. A real function f may then be expressed in terms of the surface harmonics $Y_{\ell ms}$:

$$f(p, \theta, \varphi) = \sum_{\ell=0}^{\infty}\sum_{m=0}^{\ell}\sum_{s=0}^{1}f_{\ell ms}(p)Y_{\ell ms}(\theta, \varphi). \tag{3}$$

We define the complex amplitudes $f_\ell^m(p) = \sqrt{\frac{2\ell+1}{4\pi}\frac{(\ell-m)!}{(\ell+m)!}}\frac{f_{\ell m0}(p) - if_{\ell m1}(p)}{\sqrt{2}}$ (for $m > 0$) and $f_\ell^0(p) = \sqrt{\frac{2\ell+1}{4\pi}}f_{\ell 00}(p)$ so that Eq. (3) yields:

$$f(p, \theta, \varphi) = \sum_{\ell=0}^{\infty}\left\{ P_\ell^0(\cos\theta)f_\ell^0(p) + 2\Re\left[\sum_{m=1}^{\ell}P_\ell^m(\cos\theta)f_\ell^m(p)e^{im\varphi}\right]\right\}, \tag{4}$$

where $\Re[\ldots]$ and $\Im[\ldots]$ yield the real and imaginary parts of their argument respectively. By defining f_ℓ^{-m} to be the complex conjugate of f_ℓ^m, i.e. $f_\ell^{-m} \equiv (f_\ell^m)^*$, we can write:

$$f(p, \theta, \varphi) = \sum_{\ell=0}^{\infty}\sum_{m=-\ell}^{\ell}f_\ell^m(p)P_\ell^{|m|}(\cos\theta)e^{im\varphi}. \tag{5}$$

The expressions (3)–(5) are equivalent to the cartesian tensor product expansion $\sum_{\ell ms}f_{\ell ms}Y_{\ell ms} = \sum_{\ell=0}^{\infty}\frac{\{\boldsymbol{f}_\ell\}_\ell\{\boldsymbol{p}^\ell\}}{p^\ell}$ (see [21]).

2.1.2. The Vlasov–Maxwell system of equations

The distribution of electrons in phase-space may be described by the real function $f(\boldsymbol{r}, \boldsymbol{p}, t)$, where the dependence on time t has also been included. $f(\boldsymbol{r}, \boldsymbol{p}, t)$ can be expanded to spherical harmonics in momentum-space as in Eq. (5):

$$f(\boldsymbol{r}, \boldsymbol{p}, t) = \sum_{\ell=0}^{\infty}\sum_{m=-\ell}^{\ell}f_\ell^m(\boldsymbol{r}, |\boldsymbol{p}|, t)P_\ell^{|m|}(\cos\theta)e^{im\varphi}, \qquad f_\ell^{-m} = (f_\ell^m)^*. \tag{6}$$

Thus, $f(\boldsymbol{r}, \boldsymbol{p}, t)$ is represented by the complex amplitudes $f_\ell^m(\boldsymbol{r}, p, t)$, which are functions of time t, position in configuration-space $\boldsymbol{r} = (x, y, z)$ and magnitude of momentum $p \equiv |\boldsymbol{p}|$. The spherical coordinates in momentum-space are related to the cartesian coordinates (p_x, p_y, p_z) through:

$$p = \sqrt{p_x^2 + p_y^2 + p_z^2}, \tag{7}$$

$$\theta = \arccos(p_x/p), \quad 0 \leqslant \theta < \pi, \tag{8}$$

$$\varphi = \arctan_2(p_z, p_y), \quad 0 \leqslant \varphi < 2\pi, \tag{9}$$

where $\arctan_2(p_z, p_y)$ returns the angle from the p_y-axis to the vector (p_z, p_y) in the range $[0, 2\pi]$. The converse transformation is $p_x = p\cos\theta$, $p_y = p\sin\theta\cos\varphi$, $p_z = p\sin\theta\sin\varphi$. For many physical problems of interest, especially for electron transport, the first few terms in the expansion (6) contain much of the important physics. To see this we consider moments of the distribution function and use the notation $\langle \ldots \rangle \equiv \int_{\boldsymbol{p}}(\ldots)f(\boldsymbol{r}, \boldsymbol{p}, t)d\boldsymbol{p}$:

$$\langle g \rangle = 4\pi\int_0^{\infty}gp^2f_0^0 dp, \tag{10}$$

$$\langle g\hat{\mathbf{p}} \rangle = \frac{4\pi}{3} \int_0^\infty g p^2 \begin{pmatrix} f_1^0 \\ 2\Re(f_1^1) \\ -2\Im(f_1^1) \end{pmatrix} dp, \tag{11}$$

$$\langle g\hat{\mathbf{p}}\hat{\mathbf{p}} \rangle = \frac{\langle g \rangle}{3} \mathbf{I_2} + \frac{4\pi}{15} \int_0^\infty g p^2 \begin{pmatrix} 2f_2^0 & 6\Re(f_2^1) & -6\Im(f_2^1) \\ 6\Re(f_2^1) & 12\Re(f_2^2) - f_2^0 & -12\Im(f_2^2) \\ -6\Im(f_2^1) & -12\Im(f_2^2) & -12\Re(f_2^2) - f_2^0 \end{pmatrix} dp, \tag{12}$$

where $\hat{\mathbf{p}} \equiv \mathbf{p}/p$, $\hat{\mathbf{p}}\hat{\mathbf{p}}$ a second order tensor, $\mathbf{I_2}$ the unit tensor and $g(p)$ an arbitrary function of the magnitude of momentum. The stress-energy tensor can be expressed using Eqs. (10)–(12), which are equivalent to Eqs. (10a)–(10c) in Johnston [21], and depend only on the amplitudes $f_{\ell\leqslant 2}^m$. Eqs. (10)–(12) yield quantities such as the density $n = \langle 1 \rangle$, the fluid velocity $\mathbf{V} = \langle \boldsymbol{v} \rangle/n$, the electron pressure and temperature $P_e = n \, k_B T_e = m_e \langle |\boldsymbol{v} - \mathbf{V}|^2 \rangle/3$ and the heat flux $\mathbf{q} = \frac{1}{2} m_e \langle |\boldsymbol{v} - \mathbf{V}|^2 (\boldsymbol{v} - \mathbf{V}) \rangle$.

The Boltzmann equation for the electron distribution function $f(\mathbf{r},\mathbf{p},t)$ is:

$$\frac{\partial f}{\partial t} + \boldsymbol{v} \cdot \frac{\partial f}{\partial \mathbf{r}} - e\left(\mathbf{E} + \frac{\boldsymbol{v}}{c} \times \mathbf{B}\right) \cdot \frac{\partial f}{\partial \mathbf{p}} = \left(\frac{\delta f}{\delta t}\right)_c$$

where the collision term $\left(\frac{\delta f}{\delta t}\right)_c$ will be discussed in detail in Section 3. From this point on we adopt normalized units $t \to \omega_p t$, $\mathbf{r} \to k_p \mathbf{r}$, $q \to q/e$, $m \to m/m_e$, $\boldsymbol{v} \to \boldsymbol{v}/c$, $n \to n/n_p$, $\{\mathbf{E},\mathbf{B}\} \to e\{\mathbf{E},\mathbf{B}\}/(m_e c \omega_p)$ and $f \to c^3 f/n_p$, where n_p is the plasma density, $\omega_p = \sqrt{4\pi e^2 n_p/m_e}$ the plasma frequency and $k_p^{-1} = c/\omega_p$ the skin depth. In terms of the normalized quantities the Boltzmann equation becomes:

$$\frac{\partial f}{\partial t} + \boldsymbol{v} \cdot \frac{\partial f}{\partial \mathbf{r}} - (\mathbf{E} + \boldsymbol{v} \times \mathbf{B}) \cdot \frac{\partial f}{\partial \mathbf{p}} = \left(\frac{\delta f}{\delta t}\right)_c \tag{13}$$

and Maxwell's equations become:

$$\frac{\partial}{\partial \mathbf{r}} \times \mathbf{E} = -\frac{\partial}{\partial t} \mathbf{B}, \tag{14}$$

$$\frac{\partial}{\partial \mathbf{r}} \times \mathbf{B} = \mathbf{J} + \frac{\partial}{\partial t} \mathbf{E}, \tag{15}$$

where the contribution of the electrons to the current is $\mathbf{J}(\mathbf{r},t) = -\langle \boldsymbol{v} \rangle = -n\mathbf{V}$ in normalized units.

The normalized Boltzmann Eq. (13) yields an expression for the evolution of each of the amplitudes f_ℓ^m (see Eq. (29) in Ref. [5]):

$$\frac{\partial f_\ell^m}{\partial t} - \mathcal{A}_{\ell,x}^m - \mathcal{A}_{\ell,y}^m - \mathcal{A}_{\ell,z}^m - \mathcal{E}_{\ell,x}^m - \mathcal{E}_{\ell,y}^m - \mathcal{E}_{\ell,z}^m - \mathcal{B}_\ell^m = \mathcal{C}_{\ell,i}^m + \mathcal{C}_{\ell,e}^m + \mathcal{S}, \tag{16}$$

where the terms on the right-hand-side are the contributions of angular scattering of electrons off ions $\mathcal{C}_{\ell,i}^m$, collisions between electrons $\mathcal{C}_{\ell,e}^m$, and a phenomenological laser source $\mathcal{S}$. Laser heating can be modeled by replacing a percentage of the isotropic part of the distribution f_0^0 with a "hot" distribution of electrons $(f_0^0)_{hot}$ during each time-step (see Ref. [6]). Derivation of the collision terms is deferred to Section 3. On the left-hand-side the contributions of the spatial advection $\mathcal{A}_{\ell,i}^m$, electric $\mathcal{E}_{\ell,i}^m$ and magnetic fields $\mathcal{B}_\ell^m$ are those computed by Bell et al. [5] and we present them here for completeness [36]:

For spatial advection:

$$\mathcal{A}_{\ell,x}^{m \geqslant 0} = -\upsilon \partial_x \left[\left(\frac{\ell - m}{2\ell - 1}\right) f_{\ell-1}^m + \left(\frac{\ell + m + 1}{2\ell + 3}\right) f_{\ell+1}^m \right], \tag{17}$$

$$\mathcal{A}_{\ell,y}^{m>0} + \mathcal{A}_{\ell,z}^{m>0} = -\frac{\upsilon}{2} \left[\frac{\partial_y - i\partial_z}{2\ell - 1} f_{\ell-1}^{m-1} - \frac{\partial_y + i\partial_z}{2\ell - 1}(\ell - m)(\ell - m - 1) f_{\ell-1}^{m+1} - \frac{\partial_y - i\partial_z}{2\ell + 3} f_{\ell+1}^{m-1} + \frac{\partial_y + i\partial_z}{2\ell + 3}(\ell + m + 1)(\ell + m + 2) f_{\ell+1}^{m+1} \right], \tag{18}$$

$$\mathcal{A}_{\ell,y}^0 + \mathcal{A}_{\ell,z}^0 = \Re\left\{ -\upsilon(\partial_y + i\partial_z) \left[-\frac{\ell(\ell - 1)}{2\ell - 1} f_{\ell-1}^1 + \frac{(\ell + 1)(\ell + 2)}{2\ell + 3} f_{\ell+1}^1 \right] \right\}. \tag{19}$$

For the electric field:

$$\mathcal{E}_{\ell,x}^{m \geqslant 0} = E_x \left[\frac{\ell - m}{2\ell - 1} G_{\ell-1}^m + \frac{\ell + m + 1}{2\ell + 3} H_{\ell+1}^m \right], \tag{20}$$

$$\mathcal{E}_{\ell,y}^{m>0} + \mathcal{E}_{\ell,z}^{m>0} = \frac{1}{2} \left[\frac{E_y - iE_z}{2\ell - 1} G_{\ell-1}^{m-1} - \frac{E_y + iE_z}{2\ell - 1}(\ell - m)(\ell - m - 1) G_{\ell-1}^{m+1} - \frac{E_y - iE_z}{2\ell + 3} H_{\ell+1}^{m-1} + \frac{E_y + iE_z}{2\ell + 3}(\ell + m + 1)(\ell + m + 2) H_{\ell+1}^{m+1} \right], \tag{21}$$

$$\mathcal{E}_{\ell,y}^0 + \mathcal{E}_{\ell,z}^0 = \Re\left\{ (E_y + iE_z) \left[-\frac{\ell(\ell - 1)}{2\ell - 1} G_{\ell-1}^1 + \frac{(\ell + 1)(\ell + 2)}{2\ell + 3} H_{\ell+1}^1 \right] \right\}, \tag{22}$$

where $G_\ell^m = p^\ell \partial_p(p^{-\ell}f_\ell^m)$ and $H_\ell^m = p^{-\ell-1}\partial_p(p^{\ell+1}f_\ell^m)$. To calculate the derivatives of f_ℓ^m as $p \to 0$ we can use the Taylor-expanded expressions $f_0^0(p) = f_0^0(0) + c_{00}p^2$ and $f_{\ell>0}^m(p) = c_{\ell m}p^\ell$ (see Section 2.2.1).

Finally, for the magnetic field:

$$\mathcal{B}_\ell^{m>0} = -iB_x m f_\ell^m + \frac{1}{2}\left[(\ell-m)(\ell+m+1)(B_z-iB_y)f_\ell^{m+1} - (B_z+iB_y)f_\ell^{m-1}\right], \tag{23}$$

$$\mathcal{B}_\ell^0 = \ell(\ell+1)\Re\left\{(B_z-iB_y)f_\ell^1\right\}. \tag{24}$$

Periodic and reflecting boundaries in configuration-space have been implemented in OSHUN. For the reflecting boundaries the transverse (parallel) magnetic field $\boldsymbol{B}_\perp$ ($\boldsymbol{B}_\parallel$) and the parallel (transverse) electric field $\boldsymbol{E}_\parallel$ ($\boldsymbol{E}_\perp$) must be odd (even) functions of the distance from the boundary. If the boundary is placed at some x_b (or y_b) on the x-axis (or y-axis), the reflected distribution function f_{Rx} (or f_{Ry}) is given from the expressions:

$$f_{Rx}(x_b \pm x, p_x) = f(x_b \mp x, -p_x) = \sum_{\ell=0}^{\infty}\sum_{m=-\ell}^{\ell}(-1)^{\ell+m}f_\ell^m P_\ell^{|m|}(\cos\theta)e^{im\varphi}, \tag{25}$$

$$f_{Ry}(y_b \pm y, p_y) = f(y_b \mp y, -p_y) = \sum_{\ell=0}^{\infty}\sum_{m=-\ell}^{\ell}(-1)^m f_\ell^{-m} P_\ell^{|m|}(\cos\theta)e^{im\varphi}. \tag{26}$$

2.2. Numerical method

2.2.1. Numerical grid

In configuration-space we use a cartesian mesh with equally spaced grid-points: $x_\imath = x_{min} + \imath \times \Delta x$, $\imath = 0, 1, \ldots, N_x$ and $y_\jmath = y_{min} + \jmath \times \Delta y$, $\jmath = 0, 1, \ldots, N_y$. In momentum-space: $p_i = p_0 + i \times \Delta p$, $i = 0, 1, \ldots, N$, where p_0 is typically chosen $p_0 = \Delta p/2$ and each p_i-cell contains a volume $(4\pi/3)(p_i^3 - p_{i-1}^3)$ which for large i scales as $4\pi p_i^2 \Delta p$. The most stringent Courant–Friedrichs–Lewy (CFL) stability condition for advection in momentum-space is the one associated with the smallest cell, the p_0-cell.
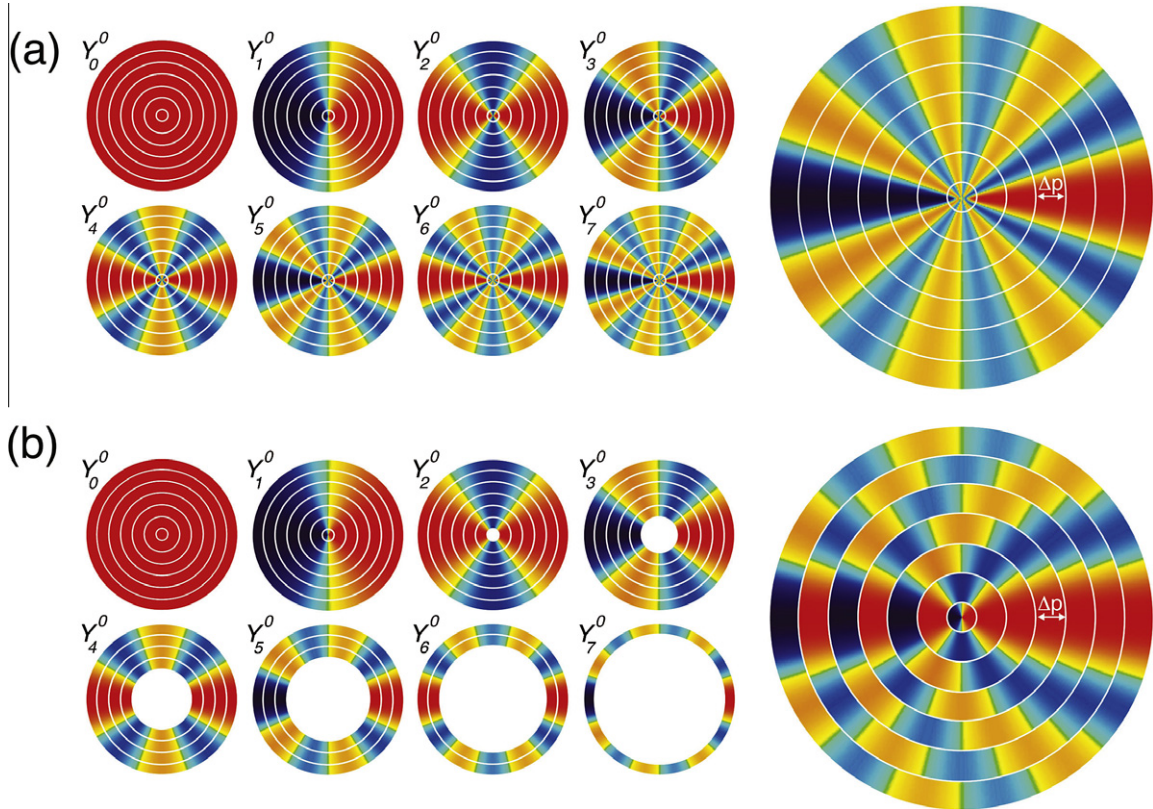

Fig. 2. An illustration of the modified grid in momentum-space. For case (a), i.e. the "un-filtered" grid, (p_x, p_y) slices of the harmonics $Y_{0\leq\ell\leq7}^0$ are shown in the first 7 cells. The size of each sector (colored blue or orange) in the p_0-cell is very small for high-order harmonics. In plot (b), i.e. the "filtered" grid, the harmonics are defined in the p_ith cell for $i \geq \ell - 1$. In (b) the smallest sector in the p_0-cell is ℓ times larger compared to the smallest sector in (a), therefore the CFL condition is ℓ times less restrictive.

To illustrate the discretization in momentum-space we present in Fig. 2(a) the (p_x, p_y) slices of the first eight harmonics with $0 \leqslant \ell \leqslant 7$ and $m = 0$. In other words, we plot the half-planes $Y_\ell^0(\theta, \varphi = 0)$ and $Y_\ell^0(\theta, \varphi = \pi)$ and join them so as to obtain Y_ℓ^0 on the entire $p_z = 0$ plane. The maximum value of $Y_\ell^0(\theta, \varphi)$, i.e. $Y_\ell^0(0,0)$, is shown with red, and blue is used for $-Y_\ell^0(0,0)$. The color-map was chosen such that positive/negative values of $Y_\ell^0(\theta, \varphi)$ are shown with warm/cold colors. The white co-centric circles drawn on top of these slices represent the p_i-cells. Fig. 2(a) shows that high-order harmonics ($\ell \geqslant 1$) essentially divide each p_i-cell to 2ℓ sectors, because $P_\ell^m(\cos \theta)$ has ℓ roots and there are two half-planes for each harmonic. Accordingly, the CFL condition depends not just on the size of the p_0-cell, but on the smallest sector within that cell, the size of which is inversely proportional to the index ℓ of the highest-order harmonic. In Fig. 2(a) we have magnified the highest order harmonic, $Y_7^0(\theta, \varphi)$, to illustrate the small sectors for low p_i-cells.

To remove this constraint we use an alternative discretization, in which fewer harmonics are resolved in the low p_i-cells and their number increases progressively for higher p_i-cells. Fig. 2(b) shows the same harmonics as Fig. 2(a), but here each harmonic is only defined for those p_i-cells for which $i \geqslant \ell - 1$. Harmonics with $m \geqslant 1$ are treated exactly as those with $m = 0$, i.e. whenever Y_ℓ^0 is defined in some p_i-cell $Y_\ell^{1 \leqslant m \leqslant \ell}$ is also defined. By combining these harmonics we obtain an illustration of the "grid" in momentum-space (magnified in Fig. 2(b)). The disparity between the sizes of the sectors in the momentum grid is thus reduced and the CFL condition is relaxed by a factor proportional to ℓ. This process amounts to filtering of the high wavenumbers in the momentum grid and it is analogous to the filtering action of the particle-shape factors in PIC codes (see discussion in Birdsall and Langdon, [8, p. 167]). To further justify this discretization, one can write the ℓth order harmonic in terms of ℓth order products of the direction cosines, which clearly shows that the amplitudes f_ℓ^m must vanish as p^ℓ when $p \rightarrow 0$. Moreover, when angular scattering is considered, high-order harmonics $\ell \geqslant 1$ decay at a rate proportional to ℓ $(\ell + 1)/(2p^3)$ (see Section 3.1).

Advection in momentum-space requires a proper boundary condition at $p = 0$. We require $f_{\ell \geqslant 1}^m(p \rightarrow 0) \sim p^\ell$ and that the isotropic part of the distribution has an extremum at $p = 0$. To calculate the coefficients of the Taylor expansion of $f_0^0(p)$ we assume that $f_0^0(p_0)$ and $f_0^0(p_1)$ lie on the parabola $f_0^0(0) + c_{00} p^2$:

$$f_0^0(p) = f_0^0(0) + (f_0^0(p_1) - f_0^0(0)) \left(\frac{p}{p_1} \right)^2, \quad f_0^0(0) = \frac{f(p_0) - f(p_1) p_0^2 / p_1^2}{1 - p_0^2 / p_1^2}, \tag{27}$$

$$f_{\ell \geqslant 1}^m(p) = f_\ell^m(p_1) \left(\frac{p}{p_1} \right)^\ell. \tag{28}$$

Using these expressions we obtain the functions $G_\ell^m(p)$, $H_\ell^m(p)$ at the momentum-space boundary $p = p_0 : G_0^0(p_0) = \partial_p f_0^0(p_0) = \frac{f_0^0(p_1) - f_0^0(p_0)}{\Delta p} \frac{1}{1 + \Delta p / (2p_0)}$, $G_{\ell \geqslant 1}^m(p_0) = 0$ and $H_{\ell \geqslant 1}^m(p_0) = (2\ell + 1)(p_0/p_1)^\ell f_\ell^m(p_1)/p_0$.

2.2.2. Code structure

In simulating the VFP-Maxwell equations the state of the system can be described by the collection of the electromagnetic fields $\boldsymbol{E}$, $\boldsymbol{B}$ and the amplitudes of the spherical harmonics f_ℓ^m. The implementation in the code relies on this collection $X(\boldsymbol{E}, \boldsymbol{B}, [f_\ell^m])$ as well as all the necessary operations that act on X and its constituent elements. The Vlasov-Maxwell part of Eqs. (14)–(16) may be written as $\partial X / \partial t = F(X)$, where the operator F includes advection in momentum-space due to the electric field, advection in configuration-space, the effect of the magnetic field, Faraday's and Ampère's laws and a phenomenological laser source. Central difference is used for the derivatives in phase-space and the discretization of Eqs. (14)–(24) is straight-forward. Runge–Kutta methods up to 4th order have so far been implemented for the explicit integration of $\partial X / \partial t = F(X)$.

A step in the iteration loop involves a list of successive operations on each harmonic, such that each operator is applied to each container of amplitudes f_ℓ^m only once. Using Eqs. (17)–(24) we find the effect that each f_ℓ^m has on its neighboring amplitudes in ℓ-m space. A list of these operations is presented in Appendix A and it is also illustrated in Fig. 3. We note that these operations are defined whenever both amplitudes are within the boundaries of the ℓ-m space, that is when $0 \leqslant \ell \leqslant \ell_0$ and $0 \leqslant m \leqslant min(m_0, \ell)$.

The Fokker–Planck collision operator is local in configuration-space and it couples all of the amplitudes f_ℓ^m in ℓ-m space. To break the interdependence between the amplitudes and allow for rapid numerical calculations we linearize the Fokker–Planck operator assuming that the anisotropic part of the distribution is a perturbation to the isotropic part f_0^0. The nonlinear collision operator for f_0^0, which has been implemented using an explicit number- and energy-conserving scheme [26], describes the relaxation of f_0^0 towards a Maxwellian due to the energy exchange between identical colliding particles. On the other hand, the collision operator for the anisotropic part of the distribution is linear with respect to $f_{\ell \geqslant 1}^m$ and it employs an implicit scheme which makes use of the updated value of f_0^0. This linear operator describes the momentum exchange, which for ionized gases with $Z > 1$ happens in a much shorter time-scale than energy relaxation. Collisions between electrons and immobile ions (angular scattering) lead to the diffusion of electrons in momentum-space and therefore to isotropization of the distribution function. Additionally, electrons scatter off the Rosenbluth potentials [38], which are potential functions calculated from the electron distribution. The collision operators will be discussed in detail in Section 3. Here we point out that for certain problems it would be extremely expensive to apply an explicit scheme for the collisions of the anisotropic part, whereas for the isotropic part, which involves only one harmonic, this is not an issue. Once the calculation of the effects of collisions has been completed the system is ready to advance to the next time-step.
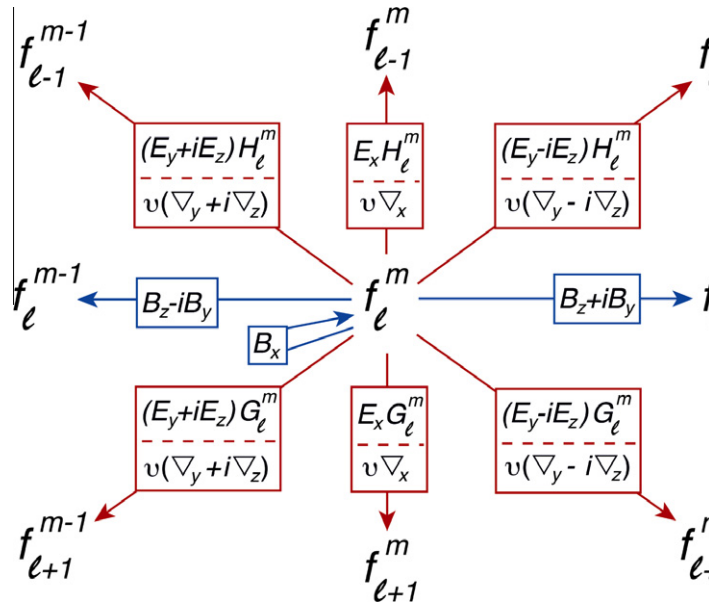
Fig. 3. A map of the operators that act on each amplitude f_ℓ^m.

The code can generate output that includes the fields, moments of f, and allows for converting the entire distribution function to a cartesian grid, which can be displayed using standard visualization software. The code is initialized with a population of stationary ions $n_i(\mathbf{r})$ determined from Gauss's law $\nabla \cdot \mathbf{E}(\mathbf{r}, t = 0) = Zn_i(\mathbf{r}) - n_e(\mathbf{r}, t)$ for some initial value of the electric field $\mathbf{E}(\mathbf{r}, t = 0)$. Parallelism is achieved by decomposing the computational domain in configuration-space in either or both x and y directions and communicating information regarding the boundaries of the state X between the different processes before each new iteration.

2.3. Vlasov simulations

For weakly anisotropic collisional plasmas few harmonics are needed to provide a high-fidelity representation of the distribution function. Thus, our code is ideally suited to investigate the effects of collisions on near-threshold instabilities. This is a testament to the fact that this is a fundamentally different approach compared to Particle-In-Cell, which is most appropriate for highly unstable/anisotropic plasmas but is much less efficient close to threshold, where it requires massive numbers of particles to suppress noise and has to employ expensive Monte-Carlo techniques to accurately account for collisions. Nevertheless, to illustrate the flexibility of our code and explore its limitations we examine two collisionless instabilities far from threshold, in regimes that involve strong electromagnetic fields, highly anisotropic distributions and trapped particles.

2.3.1. Relativistic two-stream instability

First we present simulations of the relativistic two-stream instability (see for example Ref. [32]) in the frame of the unstable wave. This instability is associated with vortices in cartesian phase-space, (x, p_x), which become increasingly complex over time as particles get trapped and oscillate around zero momentum. Hence we test the behavior of our code in the vicinity of $p = 0$, where the gradient in momentum (∇_p) exhibits a singularity and where numerical effects due to the filtered grid in Fig. 2(b)—if any—can be expected to be most pronounced.

The simulation is initialized with the distribution function:

$$f(p, \theta, x, t = 0) = \frac{0.0104 \times e^{-\frac{(p-1)^2}{2 \times 0.105^2}}}{(2\pi)^{3/2} 0.105^{3/2}} \times \left[P_0^0 + 2P_2^0(\cos\theta) + \frac{1}{50} \cos\left(\frac{2\pi x}{10}\right) P_1^0(\cos\theta) \right] + 0.04 \times H(1-p) P_0^0, \tag{29}$$

where $H(x)$ is the Heaviside step function $H(x) = \int_{-\infty}^{x} \delta(x') dx'$. To guarantee that the distribution function maintains positivity throughout the simulation we add the small pedestal value 0.04 to f for momenta $p < 1$ (note that $P_0^0 + 2P_2^0(\cos\theta) = 3\cos^2\theta \geqslant 0$). A weak current perturbation (the term $0.02 \cos\left(\frac{2\pi x}{10}\right)$) is included to seed the instability at a wavelength close to that of the most unstable mode. The boundary in configuration space is periodic. The (x, p_x) projection of $f(p, \theta, x, t = 0)$ can be seen in the first frame in either the top or bottom row in Fig. 4.

The instability is modeled in a 1D configuration, with two counter-streaming beams in the x direction. Each wavelength ($L = 10$) is resolved with 256 x-cells and 96 p-cells with $p \leqslant 3.3$. The time-step is $\Delta t = 0.02$ and the maximum time shown is $t_{max} = 30 = 1500\Delta t$. A 4th order Runge–Kutta scheme is used. The boxes in Fig. 4 have been zoomed in momentum such that
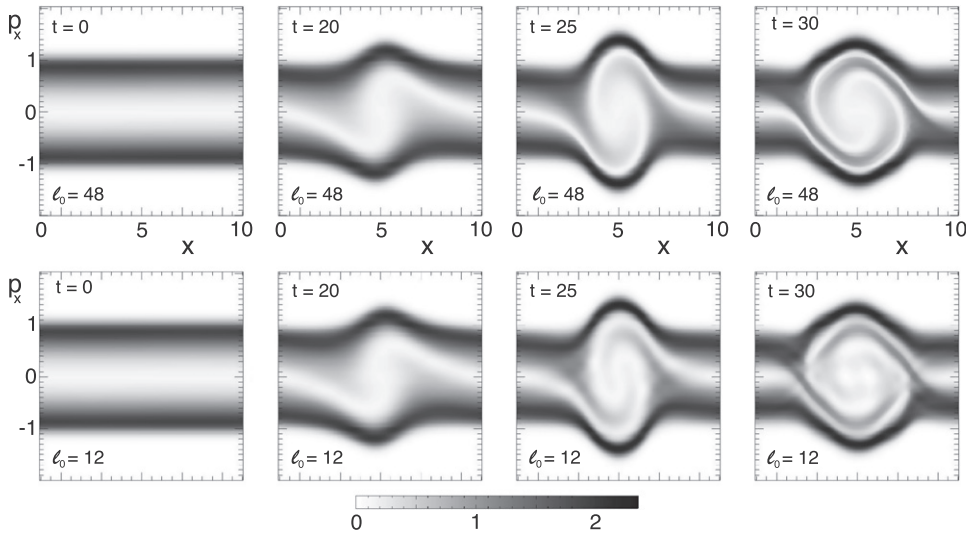
Fig. 4. The evolution of the relativistic two-stream instability in the frame of the unstable wave is shown in the top (bottom) row from a simulation with 49 (13) spherical harmonics. The boxes shown are resolved with 58 p-cells and 256 x-cells. Both simulations are initialized using Eq. (29). The simulation with $\ell_0 = 12$ reproduces the physics accurately until well into the nonlinear regime. Eventually ($t = 30$), as the structure of the distribution function becomes increasingly complex, the simulation requires a number of harmonics close to the number of p-cells to capture the fine features of the distribution. The normalization in this figure is $p_x[mc]$, $x[c/\omega_p]$, $t[\omega_p^{-1}]$ and the phase-space density $N[n_p/(mc^2/\omega_p)]$.

$p_{max} = 2$. The first simulation (first row in Fig. 4) includes 49 terms in the expansion (maximum index $\ell_0 = 48$) and the second 13 ($\ell_0 = 12$).

The first frame is identical for both simulations, and while the instability remains in the linear regime the simulations yield nearly the same results. This can be confirmed by comparing the frames at $t = 20$. Small differences show up in the nonlinear regime ($t = 25$), and over time ($t = 30$) they become considerable. For $t > 30$ negative values for the distribution function appear for both simulations as the phase-space structures continue to stretch and wrap around $p = 0$. To continue the simulation deeper in the nonlinear regime one would have to increase the resolution in phase-space and include more harmonics.

Positivity of the distribution function can only be expected as $\Delta p \to 0$ and if the spherical harmonic expansion includes all of the harmonics that have significant amplitude. We remind here that the number of harmonics kept in each p_i-cell is $\ell = i + 1$, such that near $p = 0$ the two simulations shown in Fig. 4 employ identical expansions. It is nevertheless exactly near $p = 0$ where the simulation with $\ell_0 = 12$ fails to accurately recover the physics in the nonlinear regime. This indicates that it is the lack of adequate harmonics for large $|\boldsymbol{p}|$ that causes this unphysical behavior. To confirm that the filtered grid (see Fig. 2(b)) works well we repeated the simulations using all of the spherical harmonics in the lowest momentum cells (see Fig. 2(a)) and the results were virtually indistinguishable. Lack of positivity may thus be interpreted as an indication that the expansion has been truncated too soon and at the same time that the resolution in $|\boldsymbol{p}|$ is not sufficient.

The pedestal value was used to ameliorate this problem, partly by reducing the growth rate of the two-stream instability and partly by preventing small errors from manifesting themselves as negative values for f. However, even if the pedestal value is ignored the system still exhibits reasonable behavior. One way to maintain positivity would be to derive a closure condition that would work for an arbitrary harmonic. Another possibility would be to dynamically change the resolution in $|\boldsymbol{p}|$ and the number of harmonics during the simulation. We reiterate that for collisional plasmas the complicated structures in momentum-space are smoothed out quickly, so that few harmonics and large Δp suffice, even for long simulations.

2.3.2. Relativistic current-filamentation instability

To test the code in 2D3P with electromagnetic fields in 3D and spatial advection in 2D, and to study the effect of choosing $m_0 < \ell_0$ we present simulations of the current-filamentation instability [27,48], in which two identical electron beams counter-stream perpendicularly to the simulation plane (x,y). While the natural orientation for the anisotropy axis is "x", as per Eqs. (8) and (9), to demonstrate that the code is robust and capable of handling different geometries we set the anisotropy axis in "z".

The distribution function is initialized as:

$$f(p, \theta, \varphi, x, y, t = 0) = \frac{0.0104 \times e^{-\frac{(p-1)^2}{2 \times 0.105^2}}}{(2\pi)^{3/2} 0.105^{3/2}} \times \left\{ P_0^0 - P_2^0(\cos\theta) + 2\Re\left[-\frac{1}{4} P_2^2(\cos\theta) \times e^{i2\varphi} \right] \right.$$

$$\left. + 2\Re\left[\frac{-i}{10} \cos\left(\frac{2\pi x}{10}\right) \cos\left(\frac{2\pi y}{10}\right) P_1^1(\cos\theta) e^{i\varphi} \right] \right\} + \frac{0.0824 \times e^{-\frac{(p-1)^2}{2 \times 0.33^2}}}{(2\pi)^{3/2} 0.33^{3/2}} P_0^0. \tag{30}$$
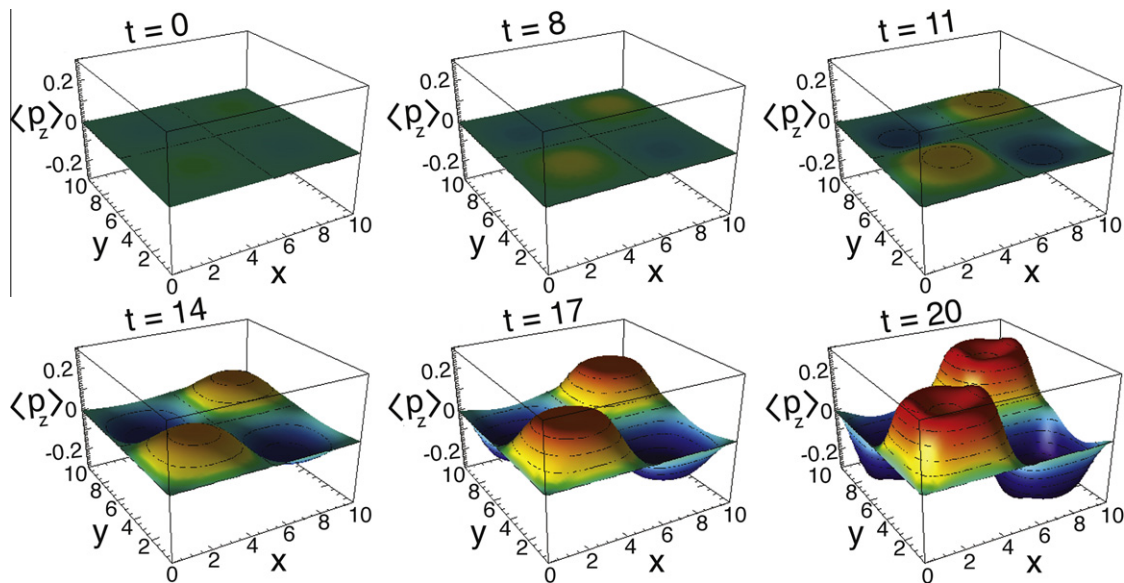
Fig. 5. Six plots of $\langle p_z \rangle(x,y)$ are presented to describe the evolution of the relativistic current-filamentation instability. The instability starts from a small initial current perturbation at $t = 0$ and is shown until well into the nonlinear regime at $t = 20$. The size of the box is equal to one wavelength of the instability in each direction. The current perturbation grows exponentially pinching the electron beams, until the instability reaches the nonlinear regime, at which point the space-charge at the center of the filaments is sufficient to prevent further focusing (see the hollow filaments at $t = 20$.) The normalization in this figure is $x\ [c/\omega_p]$, $y[c/\omega_p]$, $t[\omega_p^{-1}]$ and $p[n_p\ mc]$.

The instability is seeded by a current perturbation, $-2\Im\left[\frac{-i}{10}\cos\left(\frac{2\pi x}{10}\right)\cos\left(\frac{2\pi y}{10}\right)\right] = \frac{1}{5}\cos\left(\frac{2\pi x}{10}\right)\cos\left(\frac{2\pi y}{10}\right)$, where the perturbation wavelength is close to that of the most unstable mode in both x and y, and it is equal to the dimensions of the simulation box. The last term in Eq. (30) is a wide spherical shell in momentum-space and it serves the same purpose as the pedestal value used for the two-stream instability above, that is it ensures that the distribution function remains positive until well into the nonlinear regime (note that $P_0^0 - P_2^0(\cos\theta) - \frac{1}{2}P_2^2(\cos\theta)\cos 2\varphi = \frac{3}{2}(1 - \cos 2\varphi) = 3\sin^2\varphi \geqslant 0$). This distribution function is similar to the one used to study the two-stream instability, but because the perturbation wavevectors are perpendicular to the beams and $\partial_z \equiv 0$ the electromagnetic current-filamentation instability with primary fields B_x, B_y and E_z will grow instead of the two-stream.

The 10×10 simulation box in configuration-space is resolved with a 64×64 mesh, and 96 p-cells are used with $p \leqslant 3.3$. For the simulation shown in Fig. 5 the maximum indices are $(\ell_0, m_0) = (48, 48)$ (1225 total harmonics.) The time-step is $\Delta t = 0.15$. The boundaries in configuration space are periodic in both x and y, and in this case a 3rd order Runge–Kutta method was used.

Symmetric magnetic fields B_x and B_y and the corresponding electric field E_z grow as a result of the instability, pinching the counter-streaming electron beams at complementary locations in configuration-space as shown in Fig. 5. During the early stage of the instability the modes retain a sinusoidal shape. For this problem the generation of electric fields E_x and E_y due to the pinching of electron beams is a higher order effect [47], which means that they are small during the linear stage of the instability. As the instability enters the nonlinear regime E_x and E_y become comparable to $v_z B_y$ and $v_z B_x$, which makes pinching the electron beams more difficult and leads to a flattening of the peaks observed at $t = 17$. At $t = 20$ the filaments have the hollow profile shown in the last frame in Fig. 5. At this stage one would expect ions to start moving due to the large electric fields, however ions are stationary in the current version of the code.

The massive changes of the entire distribution function in momentum-space during the late linear and nonlinear stages were tracked by projecting the spherical harmonic expansion to a cartesian grid. Small negative values appear at some locations in the (p_x, p_y, p_z)-space after $t \simeq 16$. Using a smaller/larger pedestal value shifts this to earlier/later times. Nevertheless, for small negative values the behavior of the instability seems physical. The evolution of the distribution in the (p_x, p_y, p_z)-space is not entirely identical in the (p_x, p_z) and (p_y, p_z) planes. The consequences of this are not visible in the magnetic fields, but they are noticeable in the electric fields E_x and E_y, which become important in the nonlinear regime and are the reason for the small asymmetry between x and y directions observed for $t = 20$ in Fig. 5. This small asymmetry can be attributed to the fact that the expressions used to calculate the effect of E_x and E_y, i.e. Eqs. (20) and (21), are very dissimilar when realized in finite difference form. If the anisotropy axis is instead set to the "natural" orientation, that is the x-axis, the asymmetry in the corresponding electric fields (E_y, E_z) can be expected to vanish.

To investigate the effect of the truncation of the expansion we repeated the above simulation for many combinations of ℓ_0 and m_0. For $m_0 = \ell_0 < 10$ many of the features of the growing mode appear unphysical even in the linear regime. For $m_0 = \ell_0 = 12$ (91 harmonics) the evolution of the instability in the linear regime (not shown) is similar to that for $m_0 = \ell_0 = 48$. As the instability enters the nonlinear regime numerical artifacts show up and they become more pronounced
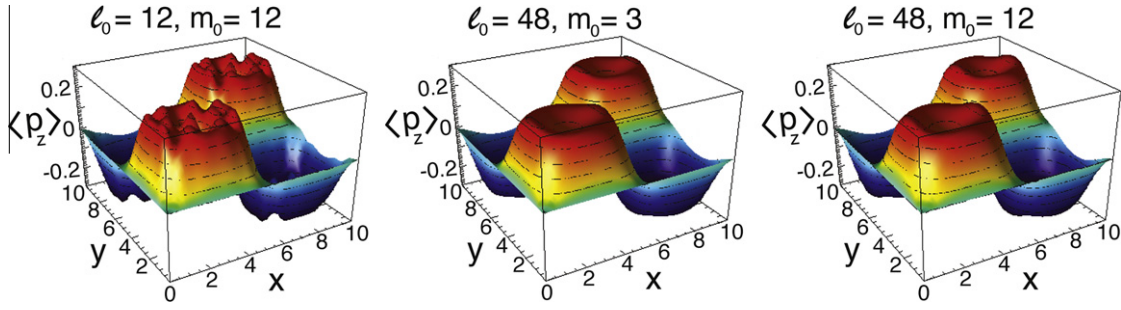
Fig. 6. $\langle p_z \rangle(x,y)$ in the nonlinear regime ($t = 20$) of the relativistic current-filamentation instability from three simulations with different number of spherical harmonics. The plot on the left corresponds to a simulation with $(\ell_0, m_0) = (12,12)$ (91 harmonics), the plot in the middle to a simulation with $(\ell_0, m_0) = (48,3)$ (190 harmonics), and the plot on the right to a simulation with $(\ell_0, m_0) = (48,12)$ (559 harmonics). This is to be compared with the last frame in Fig. 5 where $(\ell_0, m_0) = (48,48)$ (1225 harmonics). The normalization in this figure is $x\,[c/\omega_p]$, $y\,[c/\omega_p]$, $t\,[\omega_p^{-1}]$ and $p\,[n_p\,mc]$.

over time. This is shown in Fig. 6 on the left, where the filaments in $\langle p_z \rangle(x,y)$ exhibit artificial noise. By further increasing the number of harmonics (and keeping $m_0 = \ell_0$) we observe that the behavior of the instability converges to that shown in Fig. 5. For example for $m_0 = \ell_0 = 24$ (325 harmonics) the numerical noise has almost disappeared at the same point in time. Subsequently we fix $\ell_0 = 48$ and vary m_0. For $m_0 = 2$ (144 harmonics) some features of the growing mode are unphysical even in the linear regime. For $m_0 = 3$ (190 harmonics) the evolution of the instability closely mirrors that shown in Fig. 5 and even in the nonlinear regime noise is not observed (see middle plot in Fig. 6). However, the shape of the structures in the $\langle p_z \rangle(x,y)$ is artificially smoothed. Increasing the index m_0 to $m_0 = 12$ (559 harmonics, see Fig. 6) we obtain behavior indistinguishable from that in Fig. 5.

For such relativistic collisionless plasmas high-order harmonics do not decay and the lack of adequate terms in the expansion can be expected to affect the physics after some point in time. Notwithstanding, even for these cases the behavior of the instability in the linear and early nonlinear regimes can be studied using about 100 harmonics ($\ell_0 \geqslant 13$). For problems in which the instability is weaker and/or the plasma is collisional, simulations require far fewer terms in the expansion. This is left for future work, in which the collisional instabilities—especially the ones that are relevant to ICF plasmas—will be studied in detail.

3. Collisions

3.1. The linearized Fokker–Planck equation for weakly anisotropic distributions

Collisions involve predominantly low-energy particles. We assume that relativistic effects can be ignored in the collision operators and use the nonrelativistic formalism in Shkarofsky et al. [42] to calculate the evolution of a distribution f of particles with mass m and charge $q = ze$ scattering off a distribution F of particles with mass $M = \mu m$ and charge $Q = Ze$:

$$\frac{1}{\Gamma_{zZ}}\left(\frac{\delta f}{\delta t}\right) = \frac{4\pi}{\mu}Ff + \left(\frac{\mu-1}{\mu+1}\right)\nabla\mathbb{H}(F)\cdot\nabla f + \frac{\nabla\nabla\mathbb{G}(F):\nabla\nabla f}{2}, \tag{31}$$

where ∇ is the gradient in velocity space, $\Gamma_{zZ} = 4\pi(zZe^2)^2\ln\Lambda/m^2$ and $\mathbb{H}$, $\mathbb{G}$ the Rosenbluth potentials (see [38]) are integral operators for F. We expand the distribution functions F, f to an isotropic part F_0^0, f_0^0 and an anisotropic perturbation $\widetilde{F}_a, \widetilde{f}_a : F = F_0^0 + \widetilde{F}_a$, $f = f_0^0 + \widetilde{f}_a$. The equations become:

$$\frac{1}{\Gamma_{zZ}}\left(\frac{\delta f_0^0}{\delta t}\right) = \frac{4\pi}{\mu}F_0^0 f_0^0 + \left(\frac{\mu-1}{\mu+1}\right)\nabla\mathbb{H}(F_0^0)\cdot\nabla f_0^0 + \frac{\nabla\nabla\mathbb{G}(F_0^0):\nabla\nabla f_0^0}{2}, \tag{32}$$

$$\frac{1}{\Gamma_{zZ}}\left(\frac{\delta \widetilde{f}_a}{\delta t}\right) = \frac{4\pi}{\mu}\left[F_0^0\widetilde{f}_a + f_0^0\widetilde{F}_a\right] + \left(\frac{\mu-1}{\mu+1}\right)[\nabla\mathbb{H}(F_0^0)\cdot\nabla\widetilde{f}_a + \nabla f_0^0\cdot\nabla\mathbb{H}(\widetilde{F}_a)]$$
$$+ \frac{\nabla\nabla\mathbb{G}(F_0^0):\nabla\nabla\widetilde{f}_a}{2} + \frac{\nabla\nabla f_0^0:\nabla\nabla\mathbb{G}(\widetilde{F}_a)}{2}. \tag{33}$$

We use the expansion of f to spherical harmonics, $f = \sum_{\ell=0}^{\infty}\sum_{m=-\ell}^{\ell}f_\ell^m(v)P_\ell^{|m|}(\cos\theta)e^{im\varphi}$ and similarly for F. Following Shkarofsky et al. [42] we define the integrals:

$$I_j(F_\ell^m) = \frac{4\pi}{v^j}\int_0^v F_\ell^m(u)u^{j+2}du, \tag{34}$$

$$J_j(F_\ell^m) = \frac{4\pi}{v^j}\int_v^\infty F_\ell^m(u)u^{j+2}du. \tag{35}$$

Using expressions (34) and (35) the Rosenbluth potentials can be written as:

$$\mathbb{H} = \frac{1+\mu}{\mu} \sum_{\ell=0}^{\infty} \sum_{m=-\ell}^{\ell} \frac{1/\upsilon}{2\ell+1} \left[I_\ell\left(F_\ell^m\right) + J_{-1-\ell}\left(F_\ell^m\right) \right] P_\ell^{|m|}(\cos\theta) e^{im\varphi}, \tag{36}$$

$$\mathbb{G} = \sum_{\ell=0}^{\infty} \sum_{m=-\ell}^{\ell} \upsilon \left[\frac{I_{\ell+2}\left(F_\ell^m\right) + J_{-1-\ell}\left(F_\ell^m\right)}{(2\ell+1)(2\ell+3)} - \frac{I_\ell\left(F_\ell^m\right) + J_{1-\ell}\left(F_\ell^m\right)}{(2\ell-1)(2\ell+1)} \right] P_\ell^{|m|}(\cos\theta) e^{im\varphi}. \tag{37}$$

The isotropic part of the distributions F and f, i.e. F_0^0 and f_0^0, does not depend on angle and we can write $\nabla = \hat{\upsilon}\partial_\upsilon$ and $\nabla\nabla = [(\mathbf{I_2} - \hat{\upsilon}\hat{\upsilon})/\upsilon]\partial_\upsilon$ when these operators act on it. We also note that $\hat{\upsilon}\hat{\upsilon} : \nabla\nabla = \partial_\upsilon^2$ and $\mathbf{I_2} : \nabla\nabla = \nabla^2$. Exploiting these properties and substituting the Rosenbluth potentials into Eq. (32) we obtain:

$$\frac{1}{\Gamma_{zz}}\left(\frac{\delta f_0^0}{\delta t}\right) = \frac{1}{3\upsilon^2}\frac{\partial}{\partial\upsilon}\left[\frac{3}{\mu}f_0^0 I_0\left(F_0^0\right) + \upsilon\left(I_2\left(F_0^0\right) + J_{-1}\left(F_0^0\right)\right)\frac{\partial f_0}{\partial\upsilon}\right]. \tag{38}$$

To derive an equation for the high-order harmonics we note that the only operator that acts on angle in Eq. (33) is ∇^2 and it can be substituted with $-\ell\times(\ell+1)/\upsilon^2$. Calculating the derivatives ∂_υ and ∂_υ^2 of the Rosenbluth potentials and substituting them into Eq. (33) yields:

$$\begin{aligned}
\frac{1}{\Gamma_{zZ}}\left(\frac{\delta f_{\ell\geq1}^m}{\delta t}\right) &= \frac{4\pi}{\mu}\left[F_0^0 f_\ell^m + f_0^0 F_\ell^m\right] \\
&\quad - \frac{(\mu-1)}{\mu\upsilon^2}\left\{\frac{\partial f_0^0}{\partial\upsilon}\left[\frac{\ell+1}{2\ell+1}I_\ell\left(F_\ell^m\right) - \frac{\ell}{2\ell+1}J_{-1-\ell}(F_\ell^m)\right] + I_0\left(F_0^0\right)\frac{\partial f_\ell^m}{\partial\upsilon}\right\} \\
&\quad + \frac{I_2\left(F_0^0\right) + J_{-1}\left(F_0^0\right)}{3\upsilon}\frac{\partial^2 f_\ell^m}{\partial\upsilon^2} + \frac{-I_2\left(F_0^0\right) + 2J_{-1}\left(F_0^0\right) + 3I_0\left(F_0^0\right)}{3\upsilon^2}\frac{\partial f_\ell^m}{\partial\upsilon} \\
&\quad - \frac{\ell(\ell+1)}{2}\times\frac{-I_2\left(F_0^0\right) + 2J_{-1}\left(F_0^0\right) + 3I_0\left(F_0^0\right)}{3\upsilon^3}f_\ell^m \\
&\quad + \frac{1}{2\upsilon}\frac{\partial^2 f_0^0}{\partial\upsilon^2}\left[C_1 I_{\ell+2}\left(F_\ell^m\right) + C_1 J_{-\ell-1}\left(F_\ell^m\right) + C_2 I_\ell\left(F_\ell^m\right) + C_2 J_{1-\ell}\left(F_\ell^m\right)\right] \\
&\quad + \frac{1}{\upsilon^2}\frac{\partial f_0^0}{\partial\upsilon}\left[C_3 I_{\ell+2}\left(F_\ell^m\right) + C_4 J_{-\ell-1}\left(F_\ell^m\right) + C_5 I_\ell\left(F_\ell^m\right) + C_6 J_{1-\ell}\left(F_\ell^m\right)\right],
\end{aligned} \tag{39}$$

where $C_1,\ldots,C_6$ are coefficients which depend on the order of the spherical harmonic ℓ:

$$C_1 = \frac{(\ell+1)(\ell+2)}{(2\ell+1)(2\ell+3)}$$

$$C_2 = -\frac{(\ell-1)\ell}{(2\ell+1)(2\ell-1)}$$

$$C_3 = \frac{-\ell(\ell+1)/2 - (\ell+1)}{(2\ell+1)(2\ell+3)}$$

$$C_4 = \frac{-\ell(\ell+1)/2 + (\ell+2)}{(2\ell+1)(2\ell+3)}$$

$$C_5 = \frac{\ell(\ell+1)/2 + (\ell-1)}{(2\ell+1)(2\ell-1)}$$

$$C_6 = \frac{\ell(\ell+1)/2 - \ell}{(2\ell+1)(2\ell-1)}$$

The second line in Eq. (39) can be identified as the additional terms that need to be included if $M \neq m$. This term comes from the potential $\mathbb{H}$, which is associated with the dynamical friction coefficient, and becomes particularly important for the scattering of massive particles off much lighter ones ($\mu \ll 1$). The last two lines in Eq. (39) can be seen as the effect of the perturbed Rosenbluth potentials $\mathbb{H}(F_\ell^m), \mathbb{G}(F_\ell^m)$ on the isotropic part of the distribution of the scattering particles (f_0^0). Substituting $\ell = 1$ ($\ell = 2$) in Eq. (39) we recover the equation for the first (second) order cartesian tensor expansion in Shkarofsky et al. [42].

Let us consider electrons ($m = m_e, z = 1$) scattering off immobile ions and substitute $\mu \gg 1$ and $F(\upsilon) = n_i \delta(\upsilon)/(4\pi\upsilon^2)$ in Eq. (39). For $\upsilon > 0$ all integrals vanish except $I_0\left(F_0^0\right) = n_i$. The terms that survive in the second and third line cancel and Eq. (39) reduces to:

$$\left(\frac{\delta f_\ell^m}{\delta t}\right)_{ei} = -\frac{\ell(\ell+1)}{2}\times\frac{n_i \Gamma_{ei}}{\upsilon^3}f_\ell^m, \tag{40}$$

where $\Gamma_{ei} = 4\pi(Ze^2)^2 \ln\Lambda/m_e^2$. This is the expression for angular scattering of electrons and it amounts to a damping rate proportional to $\ell(\ell+1)$ as a result of which high-order harmonics ($\ell \gg 1$) decay rapidly. In Eq. (39), except for the general

"angular scattering" term that appears in the forth line, i.e. $-[\ell(\ell+1)/2]\times\left[-I_2\left(F_0^0\right)+2J_{-1}\left(F_0^0\right)+3I_0\left(F_0^0\right)\right)]/(3v^3)f_\ell^m$ and scales as $O(\ell^2)$, all other terms scale as $O(\ell^0)$.

For collisions between electrons $\mu = 1$, $z = Z = 1$, $F_0^0 = f_0^0$, $F_\ell^m = f_\ell^m$ Eq. (39) reduces to:

$$\frac{1}{\Gamma_{ee}}\left(\frac{\delta f_\ell^m}{\delta t}\right) = 8\pi f_0^0 f_\ell^m + \frac{I_2\left(f_0^0\right)+J_{-1}\left(f_0^0\right)}{3v}\frac{\partial^2 f_\ell^m}{\partial v^2} + \frac{-I_2\left(f_0^0\right)+2J_{-1}\left(f_0^0\right)+3I_0\left(f_0^0\right)}{3v^2}\frac{\partial f_\ell^m}{\partial v} - \frac{\ell(\ell+1)}{2}$$

$$\times\frac{-I_2\left(f_0^0\right)+2J_{-1}\left(f_0^0\right)+3I_0\left(f_0^0\right)}{3v^3}f_\ell^m + \frac{1}{2v}\frac{\partial^2 f_0^0}{\partial v^2}\left[C_1 I_{\ell+2}\left(f_\ell^m\right)+C_1 J_{-\ell-1}\left(f_\ell^m\right)+C_2 I_\ell\left(f_\ell^m\right)+C_2 J_{1-\ell}\left(f_\ell^m\right)\right] + \frac{1}{v^2}$$

$$\times\frac{\partial f_0^0}{\partial v}\left[C_3 I_{\ell+2}\left(f_\ell^m\right)+C_4 J_{-\ell-1}\left(f_\ell^m\right)+C_5 I_\ell\left(f_\ell^m\right)+C_6 J_{1-\ell}\left(f_\ell^m\right)\right], \tag{41}$$

where $\Gamma_{ee} = 4\pi e^4 \ln \Lambda/m_e^2$. Eq. (41) may also be derived from Eq. (10) in Shkarofsky et al. [43] by carrying out the differentiation with respect to v (and similarly for Eq. (4) in Alouani-Bibi et al. [1]).

3.2. Characteristic collisional quantities

The relaxation of an isotropic distribution due to collisions between electrons (and more generally for identical particles) is described by Eq. (38) with $\mu = 1$ which can be written as:

$$\frac{1}{4\pi\Gamma_{ee}/3}\frac{\delta f_0^0}{\delta t} = \frac{1}{v^2}\frac{\partial}{\partial v}\left\{\frac{1}{v}\frac{\partial}{\partial v}\left[f_0^0\int_0^v f_0^0 u^4 du + v^3 f_0^0\int_v^\infty f_0^0 u du - 3\int_v^\infty f_0^0 u du\int_0^v f_0^0 u^2 du\right]\right\}. \tag{42}$$

For a Maxwellian distribution $\frac{n_e}{(\sqrt{2\pi}v_t)^3}e^{-v^2/(2v_t^2)}$, a characteristic relaxation time can be defined from Eq. (42) as:

$$\tau_e = \left(\frac{4\pi\Gamma_{ee}}{3}\frac{n_e}{(\sqrt{2\pi}v_t)^3}\right)^{-1} = \frac{3\sqrt{m_e}(kT_e)^{3/2}}{4\sqrt{2\pi}ne^4\ln\Lambda} \simeq 3.44\times10^5\times\frac{(T_e[eV])^{3/2}}{n[cm^{-3}]\times\ln\Lambda}sec. \tag{43}$$

This is identical to the electron collision time in Braginskii [10, p.205]. Alternatively, $\lambda_0 \equiv \frac{9m_e^2}{4\pi e^4\ln\Lambda}$ can be used [3] instead of Γ_{ee}, where $12\pi/\lambda_0 = 4\pi\,\Gamma_{ee}/3$. In terms of the quantities used to normalize the equations in the code $\Gamma_{ee} = (\omega_p c^3/n_e)\times(k_p r_e)\ln\Lambda$, where $r_e = e^2/(m_e c^2) \simeq 2.82\times10^{-13}$ is the classical electron radius. A characteristic electron–ion collision time can be defined using Γ_{ei} and assuming quasi-neutrality $n_e \simeq Zn_i$. This yields $\tau_{ei} = \tau_e/Z$ which is the characteristic momentum isotropization time. The mean free path for a thermal electron can be defined as:

$$\lambda_{mfp} = v_t \times \tau_{ei} = \frac{9}{\sqrt{2/\pi}\ln\Lambda}\times\lambda_D. \tag{44}$$

The Coulomb logarithm $\ln\Lambda$ is a weak function of the number of particles in a Debye sphere and its classical value is $\ln\Lambda = \ln(9N_D/Z)$. For hot plasmas ($T_e > 4.2\times10^5$ K $\simeq 36.2$ eV) the classical value for Λ must be reduced due to quantum mechanical effects. Using the formulas from [20] for the Coulomb logarithm we have:

$$\ln\Lambda_{ee} = 23.5 - \ln(n_e^{1/2}T_e^{-5/4}) - [10^{-5} + (\ln T_e - 2)^2/16]^{1/2}, \tag{45}$$

$$\ln\Lambda_{ei} = 23 - \ln\left(n_e^{1/2}ZT_e^{-3/2}\right), \quad T_i m_e/m_i < T_e < 10Z^2\ eV, \tag{46}$$

$$\ln\Lambda_{ei} = 24 - \ln\left(n_e^{1/2}T_e^{-1}\right), \quad T_i m_e/m_i < 10Z^2\ eV < T_e. \tag{47}$$

3.3. Numerical scheme for electron–electron collisions

3.3.1. Energy-conserving numerical scheme for the relaxation of an isotropic system of electrons
The nonlinear Eq. (42) for the relaxation of the isotropic part of a distribution of electrons may written as:

$$\left(\frac{\delta f_0^0}{\delta t}\right)_{ee} = \frac{4\pi\Gamma_{ee}}{3}\frac{1}{v^2}\frac{\partial}{\partial v}\left[\frac{1}{v}\frac{\partial W(v)}{\partial v}\right], \tag{48}$$

$$W(v) = f_0^0\int_0^v f_0^0 u^4 du + v^3 f_0^0\int_v^\infty f_0^0 u du - 3\int_v^\infty f_0^0 u du\int_0^v f_0^0 u^2 du. \tag{49}$$

This formulation allows for a numerical scheme that conserves electron energy and number density [9]. In finite difference form Eq. (48) becomes:

$$\frac{\delta f_n}{\delta t} = \frac{4\pi\Gamma_{ee}}{3}\frac{1}{v_n^2}\frac{1}{\Delta_n}\left[\frac{1}{v_{n+\frac{1}{2}}}\frac{W_{n+1}-W_n}{\Delta_{n+\frac{1}{2}}} - \frac{1}{v_{n-\frac{1}{2}}}\frac{W_n-W_{n-1}}{\Delta_{n-\frac{1}{2}}}\right], \tag{50}$$

where f_n is used to denote $f_0^0(v_n)$, $v_{n+\frac{1}{2}} = \frac{1}{2}(v_n + v_{n+1})$, $\Delta_n = \frac{1}{2}(v_{n+1} - v_{n-1})$, $\Delta_{n+\frac{1}{2}} = v_{n+1} - v_n$ and $W_n \equiv W(v_n)$ to be evaluated using Eq. (49). To calculate $\delta f_0/\delta t$ we set $v_{-1} = 0$, which yields $W_{-1} \equiv W(0) = 0$. We define the discrete nonrelativistic number

density and energy density integrals as $\mathbb{N} \equiv \sum_{n=0}^{N} f_n v_n^2 \Delta_n$ and $\mathbb{E} \equiv \sum_{n=0}^{N} f_n v_n^4 \Delta_n$ respectively. For these integrals Eq. (50) yields $\frac{\delta \mathbb{N}}{\delta t} = \frac{4\pi \Gamma_{ee}}{3} \frac{W_N - W_{N-1}}{v_{N-\frac{1}{2}} \Delta_{N-\frac{1}{2}}}$ and $\frac{\delta \mathbb{E}}{\delta t} = \frac{4\pi \Gamma_{ee}}{3} v_{N-1}^2 \frac{W_N - W_{N-1}}{v_{N-\frac{1}{2}} \Delta_{N-\frac{1}{2}}}$. Assuming that the distribution function vanishes in the vicinity of the maximum momentum we obtain $\frac{\delta \mathbb{N}}{\delta t} = 0$ and $\frac{\delta \mathbb{E}}{\delta t} = 0$. These expressions are identically true if the boundary condition at v_N is chosen such that $W_N = W_{N-1}$.

For large velocities Eq. (49) can be discretized using any standard expression for the integrals, e.g. the composite trapezoidal rule for non-uniform intervals $\int_0^v f u^4 du \to \sum_{\kappa=1}^{n} \frac{1}{2} (f_\kappa v_\kappa^4 + f_{\kappa-1} v_{\kappa-1}^4) \Delta_{\kappa-\frac{1}{2}}$. When v is small compared to the characteristic velocity of the distribution function around $v \simeq 0$ the second and the third terms in Eq. (49) cancel up to $O(v^5)$. This must be captured by the numerical scheme if the distribution function is to relax to a Maxwellian. Therefore, for velocity v below some velocity v_c, $W(v)$ is calculated using the Taylor expansion $f_n = f(0) + [f_1 - f(0)](v_n^2/v_1^2)$, where $f(0) = (f_0 - f_1 v_0^2/v_1^2)/(1 - v_0^2/v_1^2)$ as in Eq. (27). This yields:

$$W(v_n < v_c) = f_n \times \left[f(0) \frac{v_n^5}{5} + (f_1 - f(0)) \frac{v_n^7}{7 v_1^2} \right] + \left[(f_n - f(0)) v_n^3 + (f_1 - f(0)) \frac{3 v_n^5}{5 v_1^2} \right] \times \sum_{\kappa=n+1}^{N} \frac{1}{2} (f_\kappa v_\kappa + f_{\kappa-1} v_{\kappa-1}) \Delta_{\kappa-\frac{1}{2}}, \quad (51)$$

$$W(v_n \geqslant v_c) = f_n \sum_{\kappa=1}^{n} \frac{1}{2} (f_\kappa v_\kappa^4 + f_{\kappa-1} v_{\kappa-1}^4) \Delta_{\kappa-\frac{1}{2}} + v_n^3 f_n \sum_{\kappa=n+1}^{N} \frac{1}{2} (f_\kappa v_\kappa + f_{\kappa-1} v_{\kappa-1}) \Delta_{\kappa-\frac{1}{2}} - 3 \left[\sum_{\kappa=n+1}^{N} \frac{1}{2} (f_\kappa v_\kappa + f_{\kappa-1} v_{\kappa-1}) \Delta_{\kappa-\frac{1}{2}} \right]$$
$$\times \left[\sum_{\kappa=1}^{n} \frac{1}{2} (f_\kappa v_\kappa^2 + f_{\kappa-1} v_{\kappa-1}^2) \Delta_{\kappa-\frac{1}{2}} \right], \quad (52)$$

where for $v_n < v_c$ we have $f_n - f(0) = O(v_n^2)$ and therefore $W(v_n < v_c) = O(v_n^5)$. Eqs. (51)-(52) do not involve any assumptions regarding the distribution function and they do not affect the number/energy conservation properties of the numerical scheme. Eq. (51) is typically used only for the first few cells in momentum-space. One recipe for choosing v_c is to consider the coldest electron population in the system with thermal velocity $v_{t,min}$ and set $\frac{3}{2} \Delta v < v_c \lesssim v_{t,min}$ (an example is given later in this section.) For realistic problems, where the grid in momentum-space must be as small as possible, 2 to 3 grid-points will be used to resolve $v_{t,min}$ in which case expression (51) may only be used for the first 2 cells.

The final finite difference scheme is described by Eqs. (50)–(52) and a standard 4th order Runge–Kutta scheme is used for integration in time. Because this only involves one harmonic and a few simple calculations it does not affect the overall performance of the code, even if the time-step for electron–electron collisions is a fraction of the time-step used for the Vlasov part of the code.
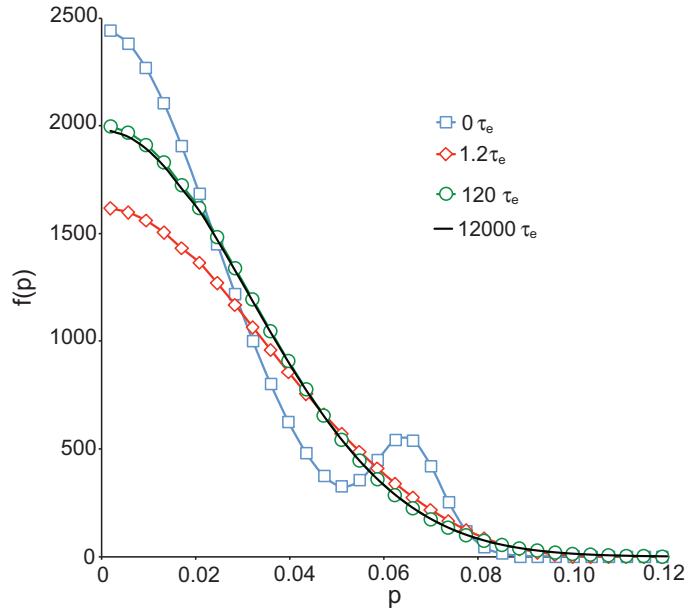

Fig. 7. The evolution of a bump-on-tail distribution of electrons under the influence of electron–electron collisions is shown for up to $12000\tau_e$ from a simulation using the conservative numerical scheme described in the text. The shapes represent the discretization in momentum-space. The distribution function is shown initially with squares (at $t = 0\tau_e$) and subsequently with rhombi (after $1.2\tau_e$), circles (after $120\tau_e$) and with a solid line (after $12000\tau_e$). The last curve, for $12000\tau_e$, overlaps almost perfectly with the curve for $120\tau_e$, because by $t = 120\tau_e$ the distribution has already relaxed to a Maxwellian. The normalization in this figure is $p[mc]$, $f[n_p/c^3]$.

Eq. (42) may also be integrated using a non-conservative method [30,16], but when this was tried in our code the distribution function, even when initialized as a Maxwellian, was visibly modified by numerical effects within a few collision times. This can be mitigated by using ultra-fine resolution in momentum-space, but such a grid would require a very small time-step and an enormous amount of computer memory. For problems such as shock ignition where the simulation time can be expected to exceed $10^4\tau_e$, this would become unfeasible. The numerical scheme presented above removes this concern for any value of N_D and makes it possible to efficiently simulate dense low-temperature plasmas.

To demonstrate that this numerical scheme makes the electron distribution relax to a Maxwellian, and that it allows for hydrodynamic time-scales to be modeled, we present in Fig. 7 the evolution of a bump-on-tail (a shell-on-tail in spherical coordinates) distribution of electrons over 10^4 collision times under the influence of electron–electron collisions exclusively. The initial background thermal velocity is set to $p_t = 0.024$ and the cell-size in momentum-space is set to $\Delta p = 3.77976 \times 10^{-3}$, i.e. there are 6 cells between 0 and p_t. Expression (51) was used for the first 5 cells and Eq. (52) for all cells beyond that. A small distortion of the distribution function due to the transition between the two different methods for calculating W_n was observed between cells #5 and #6, but for most practical purposes it can be ignored.

The evolution of the distribution of electrons close to the origin $f(v \to 0)$ can be described with the expression $\delta f/\delta t = 4\pi\Gamma_{ee}\left\{[f(0)]^2 + f''(0)\int_0^\infty f(u)udu + O(v^2)\right\}$, where the prime denotes differentiation with respect to v. We initialize a bump-on-tail distribution $f(v)$ with the values represented by the blue squares in Fig. 7. f has a maximum at the origin so $f'(0) < 0$ and because of the bump-on-tail structure the integral $\int_0^\infty f(u)udu$ is large and the origin starts falling ($\delta f(0)/\delta t < 0$). Electrons that were close to the origin move to higher velocities and the bump is smeared out. After $t = 1.2\tau_e$ the values on the momentum grid are those shown with the red rhombi. Here, f is smooth but it doesn't have the required final shape; the origin is fairly flat so that $|f'(0)|$ is small and $\delta f(0)/\delta t > 0$. The origin starts moving up again until f reaches the desired shape $f \sim e^{-p^2/(2p_t^2)}$. By the time $t = 120\tau_e$ the distribution has reached the shape shown with the green circles, which is indistinguishable from a Maxwellian with $p_t = 0.0318$, and it retains this shape over time. The solid black line confirms that f remains Maxwellian after 12000 collision times. The energy in this simulation was perfectly conserved.

3.3.2. Numerical scheme for the anisotropic part of the distribution function

For electron–electron collisions of the anisotropic part of the distribution we need to discretize Eq. (41). The finite difference form of the derivatives of f_ℓ^m is:

$$\frac{\partial f_\ell^m}{\partial v}\Big|_{v_n} = \frac{1}{2\Delta_n}f_\ell^m(v_{n+1}) - \frac{1}{2\Delta_n}f_\ell^m(v_{n-1})$$

$$\frac{\partial^2 f_\ell^m}{\partial v^2}\Big|_{v_n} = \frac{1}{\Delta_n\Delta_{n+\frac{1}{2}}}f_\ell^m(v_{n+1}) + \left(-\frac{1}{\Delta_n\Delta_{n+\frac{1}{2}}} - \frac{1}{\Delta_n\Delta_{n-\frac{1}{2}}}\right)f_\ell^m(v_n) + \frac{1}{\Delta_n\Delta_{n-\frac{1}{2}}}f_\ell^m(v_{n-1})$$

The terms associated with these derivatives form a tri-diagonal matrix. To include the terms related to the integrals $I_j(f_\ell^m(v_n))$ and $J_j(f_\ell^m(v_n))$ we write:

$$\frac{I_j(f_\ell^m(v_n))}{4\pi} = \begin{pmatrix} \frac{1}{2}\left(\frac{v_0}{v_n}\right)^j v_0^2\Delta_{\frac{1}{2}} \\ \left(\frac{v_1}{v_n}\right)^j v_1^2\Delta_1 \\ \vdots \\ \left(\frac{v_{n-1}}{v_n}\right)^j v_{n-1}^2\Delta_{n-1} \\ \frac{1}{2}v_n^2\Delta_{n-\frac{1}{2}} \\ 0 \\ \vdots \\ 0 \end{pmatrix}^T \cdot \begin{pmatrix} f_\ell^m(v_0) \\ \vdots \\ f_\ell^m(v_N) \end{pmatrix}, \qquad \frac{J_j(f_\ell^m(v_n))}{4\pi} = \begin{pmatrix} 0 \\ \vdots \\ 0 \\ \frac{1}{2}v_n^2\Delta_{n+\frac{1}{2}} \\ \left(\frac{v_{n+1}}{v_n}\right)^j v_{n+1}^2\Delta_{n+1} \\ \vdots \\ \left(\frac{v_{N-1}}{v_n}\right)^j v_{N-1}^2\Delta_{N-1} \\ \frac{1}{2}\left(\frac{v_N}{v_n}\right)^j v_N^2\Delta_{N-\frac{1}{2}} \end{pmatrix}^T \cdot \begin{pmatrix} f_\ell^m(v_0) \\ \vdots \\ f_\ell^m(v_N) \end{pmatrix}, \tag{53}$$

where the superscript "T" denotes the transpose matrix. The integral $I_j(f_\ell^m(v_n))$ leads to a lower triangular matrix and the integral $J_j(f_\ell^m(v_n))$ to an upper triangular matrix. Using this discretization one can obtain the total (dense) matrix $\boldsymbol{M}_\ell$ and accordingly $f_\ell^m(t) = (\boldsymbol{I} - \Delta t\boldsymbol{M}_\ell)f_\ell^m(t + \Delta t)$. In the following section we test the algorithm for the anisotropic part of the distribution by reproducing the Spitzer-Härm heat conduction.

3.4. The hydrodynamics limit: Spitzer-Härm heat conduction

In the classic paper by Spitzer and Härm [44] the rate of heat flow per unit area $\boldsymbol{q} = \frac{1}{2}m_e\langle|\boldsymbol{v} - \langle\boldsymbol{v}\rangle|^2(\boldsymbol{v} - \langle\boldsymbol{v}\rangle)\rangle$ due to a small temperature gradient ∇T is shown to be $\boldsymbol{q} = -K\nabla T$, where $K = \frac{20m_e^2 k(\sqrt{3kT/m_e})^5}{3e^4 Z \ln\Lambda}\left(\frac{2}{3\pi}\right)^{3/2}\delta_T$ is the heat transport coefficient. For a steady-state temperature gradient an electrostatic field builds up so as to cancel the current, thereby reducing the rate of heat flow. The effective coefficient of heat conduction κ becomes $\kappa = \epsilon K = \left(1 - \frac{\delta_E\gamma_T}{5\delta_T\gamma_E}\right)K$, where values for $\gamma_E, \gamma_T, \delta_E, \delta_T, \epsilon$ can be found in Table III in Spitzer and Härm [44]. Using the expression (44) for the mean free path we can write $\boldsymbol{q}$ as:

$$\frac{\boldsymbol{q}}{nm_e\upsilon_t^3} = -\left(\frac{320}{3\pi}\delta_T\epsilon\right)\lambda_{mfp}\frac{\nabla T}{T}. \tag{54}$$

We can define the characteristic length of temperature variation as $L^{-1} = |\nabla T|/T$ and the free streaming heat flow $q_F = nkT\upsilon_t$ to obtain:

$$\ln\left(\frac{|\boldsymbol{q}|}{q_F}\right) = -\ln\left(\frac{L}{\lambda_{mfp}}\right) + \ln\left(\frac{320}{3\pi}\delta_T\epsilon\right). \tag{55}$$

Eqs. (54) and (55) include both electron–ion and electron–electron collisions.

To simulate heat conduction and calculate the coefficient κ we add a small sinusoidal perturbation to the temperature of a quiescent plasma $n = 10^{23}/cc$, $T(x) = 298\ eV + 12.5\ eV \times [1 + \sin(2\pi x/10^4)]$. The length of temperature variation L is much longer than the mean free path $L > 10^4\lambda_{mfp}$ and the time-step $\Delta t \simeq 0.0031\tau_e$. 108 cells are used in momentum-space with $p_{max} = 6p_t$. We scan the ionization states $Z = 1, 2, 4, 16$, first using a numerical scheme that relies on the full Eq. (41), and then using the tri-diagonal matrices obtained by neglecting the integrals $I_j(f_{\ell>0}^m)$, $J_j(f_{\ell>0}^m)$ [3]. Electron–electron collisions for the isotropic part of the distribution are always included, so that the distribution function can relax to a Maxwellian. The heat conduction reaches steady-state after about $10\tau_e$, and measurements for the coefficient κ, taken after $30\tau_e$, are shown in Table 1. These values for κ are averaged over the entire simulation box so as to sample many different temperature gradients. As expected the variance of $\kappa(x)$ over x is negligible.

Excellent agreement with the values from Spitzer and Härm [44] is achieved when the full Eq. (41) and the expression (47) for $\ln\Lambda_{ei}$ are used. For high ionization states, e.g. $Z = 16$, the accuracy can be improved by using a smaller time-step to resolve the electron–ion collision time more finely, however, even with $\Delta t \sim 0.05\tau_{ei}$ (Table 1, $Z = 16$, first row) the error is less than 2%. For such high values of Z angular scattering dominates and using the full Eq. (41) may unduly slow down our code. Neglecting the integrals $I_j(f_{\ell>0}^m)$, $J_j(f_{\ell>0}^m)$ is safe for high Z, but it leads to noticeable error for small Z, e.g. for $Z = 1$ the error reaches 5%. Furthermore, keeping the integrals $I_j(f_{\ell>0}^m)$, $J_j(f_{\ell>0}^m)$ is necessary to conserve total momentum and will be particularly important when ion motion is included in future versions of the code. Bell [3] dropped the integrals $I_j(f_{\ell>0}^m)$, $J_j(f_{\ell>0}^m)$ and substituted the total scattering term $-\frac{\ell(\ell+1)}{2} \times \left(Z + \frac{-I_2(f_0^0)+2J_{-1}(f_0^0)+3I_0(f_0^0)}{3n_e}\right)\frac{n_e\Gamma_{ee}}{\upsilon^3}f_\ell^m$ with $-\frac{\ell(\ell+1)}{2} \times (Z+1)\frac{n_e\Gamma_{ee}}{\upsilon^3}f_\ell^m$. This assumption leads to errors 12.5%, 8.6% and 5.1% for κ when $Z = 1,2$ and 4 respectively, while for $Z = 16$ the error is negligible. An improvement is found by using $Z + 0.6$ instead of $Z + 1$, which for $Z = 1,2,4$ recovers κ with accuracy 0.9%,1.0% and 0.2% respectively. Finally, if the contribution of electron–electron collisions from Eq. (41) is neglected and only angular scattering and electron–electron collisions for the isotropic part of the distribution are included, the error for κ will be 22% when $Z = 16$ and will exceed 100% when $Z = 1$.

The asterisk used for the values of κ for $Z = 16$ is to draw attention to the fact that for such high Z a more appropriate expression for the Coulomb logarithm is Eq. (46). If this expression is used, instead of Eq. (47), the coefficient κ will be 30% larger. Moreover, an exact expression for the Coulomb logarithm ought to be a function of electron momentum, since the impact parameter ratio—which determines the Coulomb logarithm—depends on momentum. These issues do not indicate errors in the code or the numerical method; rather they show the sensitivity of the problem to the way $\ln\Lambda$ is defined. Another related source of inaccuracy at medium/high Z, which also derives from the problem definition rather than the numerical method, is the state of ionization, exact knowledge of which may often be inadequate. Nevertheless, for low Z the computational method can have significant impact on the physics and using the expression involving all of the terms in Eq. (41) is necessary. The simulations above were repeated by setting the temperature gradient in the y-direction and the results for the effective heat conduction coefficient were identical to those presented in Table 1.

4. Conclusions

4.1. Applicability and limitations

4.1.1. Applicability and limitations of the collision operator

A detailed study of Fokker–Planck approaches involving different approximations for the Rosenbluth potentials was presented by Alouani-Bibi et al. [1]. The linearized operator in Eq. (41) is equivalent to what Alouani-Bibi et al. [1] refer to as

Table 1

The effective heat conduction coefficient from a set of simulations with $n = 10^{23}/cc$, $T = 298\ eV + 12.5\ eV \times [1 + \sin(2\pi x/10^4)]$ and $Z = 1, 2, 4, 16$ using all of the terms in Eq. (41) (first row) or only the tri-diagonal terms (second row), i.e. neglecting the integrals $I_j(f_{\ell>0}^m)$, $J_j(f_{\ell>0}^m)$. The results are averaged over the entire simulation box, the time-step is $\Delta t \simeq 0.0031\tau_e$ and measurements are taken after $\sim 30\tau_e$, long after the heat transport has reached steady-state. Eq. (41) yields excellent agreement with classical Spitzer–Härm heat conduction for each Z (the small deviation for high Z, where $\Delta t \simeq 0.05\tau_{ei}$, can be corrected by using a smaller time-step). The reduced expression in the second row leads to error up to 5% for $Z = 1$. Expression (47) was used for $\ln\Lambda_{ei}$ everywhere. The asterisk is to indicate that for $Z = 16$ a more appropriate expression for $\ln\Lambda_{ei}$ is Eq. (46).

	$Z = 1$	$Z = 2$	$Z = 4$	$Z = 16$
Spitzer–Härm heat conduction	$\kappa = 3.20$	$\kappa = 4.96$	$\kappa = 6.98$	$\kappa = 10.63$
Eq. (41)	3.21	4.93	7.00	10.82*
Tri-diagonal terms	3.04	4.75	6.81	10.71*

"semi-anisotropic Rosenbluth potentials". Among their key findings was that this operator agrees very well with the fully nonlinear Fokker–Planck operator even for strongly anisotropic plasmas. In addition, our finite-differencing scheme conserves energy and number density exactly. Moreover, because both the explicit and implicit parts of the collision operator are local in configuration-space, they can be written as a set of repeated operations on 1D arrays that describe $f_\ell^m(x, y)$ as a function of $|\boldsymbol{p}|$. The utilization of the energy-conserving numerical scheme, which allows us to use a modest grid in momentum-space, makes it possible for these arrays to fit in the CPU cache thus further boosting the performance of the collision operator.

For the anisotropic part of the distribution, even though the inclusion of the perturbed Rosenbluth potentials to the collision operator allows for Eqs. (39) and (41) to conserve momentum, their finite-difference realization does not. This can become an issue in highly collisional plasmas, where the collision time is very short and small differencing errors can lead to considerable deviation from momentum conservation. At the moment the code uses stationary ions, but once ion motion is incorporated in future versions of the code, momentum conservation will be ensured by adding the corresponding differencing error to the ions. One could instead distribute the error amongst electrons, but because most electrons have very low energy and are highly collisional, this momentum would be immediately transferred to the ions anyway.

Plasmas irradiated by short intense lasers can become highly anisotropic in momentum-space. The degree of anisotropy depends on many factors, such as the laser intensity and the distance from the laser-plasma interface. For pulses with normalized vector potential $a_0 \equiv eA_L/(mc^2) \gtrsim 1$ the absorption process depends on the details of the particle trajectories around the laser-plasma interface. Using a heat source instead of self-consistently resolving the particle motion in the laser fields may then be an oversimplification. Furthermore, the stopping of fast particles generated by such processes may not be described by the nonrelativistic Fokker–Planck operator. For example it was recently shown by Duclous et al. [18] that in plasmas composed by a relativistic beam and a cold collisional background hard collisions can significantly impact the energy exchange between the two populations. Therefore, two directions for improving the collision operator are inclusion of relativistic effects, and implementation of a fast algorithm for the fully nonlinear Fokker–Planck collision operator.

4.1.2. Time-step

The formulation for the Vlasov part of the code in Section 2 is fully relativistic and kinetic, and it is in principle valid so long as the Vlasov description of the plasma holds. In Section 2.3 we discussed how complex structures in the phase-space of collisionless plasmas can be modelled using many high-order harmonics and high resolution in momentum-space. The constraints due to the CFL condition were also addressed and it was argued that they can be relaxed by using a filtered grid in momentum-space.

As a result of this filtered grid the time-step for transport problems is typically limited by the need to resolve plasma oscillations. This restriction can be expressed as $\omega_p \Delta t < \mathcal{C}$, where $\mathcal{C} = O(1)$ is a constant that depends on the order of the Runge–Kutta method and in preliminary tests is between 1 and 3. To avoid having to resolve plasma oscillations one needs to make the electric field implicit. However, in order for the effect of collisions to be calculated accurately the time-step must still be smaller than the collision time $\Delta t = \alpha_I \tau_{ei}$, where $0 < \alpha_I < 1$. The collision time can be expressed as $\omega_p \tau_{ei} = \frac{9}{\sqrt{2/\pi}} \frac{N_D}{Z \ln \Lambda}$, which for $Z = 1$, $T = 300$ eV and $n = 10^{23}/cc$ yields $\omega_p \tau_{ei} \simeq 100$. For a plasma under these conditions the implicit time-step would be longer than the explicit one by a factor $\sim 100 \, \alpha_I/\mathcal{C}$. Given the ratio of the computational cost of the implicit step over that of the explicit step $r_I > 1$ one obtains a speedup factor of $\sim 100 \, \alpha_I/(r_I \mathcal{C})$. For the example above, in which $N_D \sim 30$, the speed-up may not be large enough to justify using an implicit electric field. An implicit algorithm is more effective for plasmas with larger number of particles in a Debye sphere.

4.2. Comparison with other methods and plans for further development

The development of OSHUN can be viewed as part of the evolution of Vlasov–Fokker–Planck methods that has taken place over the past 30 years. OSHUN inherits the ability of other VFP codes, e.g. IMPACT by Kingham and Bell [22], to reliably and efficiently model electron transport, and it enhances it by allowing for distribution functions that exhibit significant structure in momentum-space, such as can be generated by short intense laser pulses. Moreover, because it is relativistic, it can capture the behavior of hot tails which often develop in the momentum distribution of laser-irradiated plasmas. On the other hand, mature VFP codes, such as IMPACT, already contain features that have not yet been incorporated in our code, for example ion motion and implicit time integration. Furthermore, even though OSHUN can account for external magnetic fields, such tests have not been carried out yet. Ion motion can be included either by assuming hydrodynamic ions, or by extending our current VFP model to include multiple species and using the full expression for the collision operator (39). An implicit algorithm for the electric field will be presented elsewhere. These features will enable simulations over longer time scales.

The inclusion of an arbitrary number of terms to the spherical harmonic expansion, means that our VFP code may be used for similar problems as conventional Vlasov codes [12], exhibiting many of the same advantages and limitations (compared to PIC). For collisionless problems with strongly cartesian features, such as the two-stream instability discussed earlier, cartesian Vlasov codes, especially those that employ shock-capturing techniques, should be superior to our approach. However, for collisional—even weakly collisional—plasmas our method can be very powerful, because the harmonic expansion is naturally truncated. We envision our VFP code tackling basic plasma physics problems in many different geometries, and for this reason we have included the full 3D electromagnetic fields. OSHUN will be extended to full 3D within the framework presented above.

4.3. Summary

A relativistic 2D3P Vlasov–Fokker–Planck code (OSHUN) has been developed to study plasmas under extreme conditions of temperature and pressure. The full spherical harmonic expansion of the electron distribution function in momentum-space has been implemented using the KALOS formalism [5] to allow us to treat arbitrary degrees of anisotropy, and this was illustrated with simulations of highly unstable relativistic plasmas. OSHUN reproduces efficiently the physics in the linear regime of the instability. In the nonlinear regime, an increasing number of harmonics is required to capture the physics.

The regimes in which the power of our approach is exemplified involve collisional and/or weakly anisotropic plasmas. Thus, OSHUN is ideally suited for electron transport problems and for near-threshold instabilities. This is because angular scattering leads to the decay of the high-order harmonics at a rate proportional to $\ell \times (\ell + 1)$, where the index ℓ characterizes the degree of anisotropy of a harmonic. Electron–electron collisions further enhance the rate of isotropization. The energy-conserving numerical scheme used for electron–electron collisions allows us to employ low resolution in momentum-space and perform simulations in hydrodynamic time-scales accurately and efficiently. The linearized Fokker–Planck operator for the anisotropic part of the distribution function enables modeling the transport physics with excellent accuracy.

In this article we have laid out the formalism and the structure of this new Vlasov–Fokker–Planck code. Its versatility as well as its limitations have been elucidated with simulations of basic plasma physics problems in challenging parameter spaces. Our immediate plan is to apply this code to the study of electron transport, stability and symmetry for shock ignition targets and to investigate resistive collimation and transport for fast ignition.

Acknowledgements

Appendix A. Equations for the effect of electromagnetic fields and spatial advection on f

Starting from Eqs. (17)–(24) we seek a set of equivalent expressions that can be straightforwardly implemented in a computer code. To find the effect of the electric field on the distribution function we need to calculate $G_\ell^m(f_\ell^m, \partial_p f_\ell^m)$, $H_\ell^m(f_\ell^m, \partial_p f_\ell^m)$ for each harmonic and substitute them into the equations for $\mathcal{E}_\ell^m = \mathcal{E}_{\ell,x}^m + \mathcal{E}_{\ell,y}^m + \mathcal{E}_{\ell,z}^m$. In all of the expressions below ℓ and m must be chosen so that the subscript (the ℓ-index) is larger than or equal to the superscript (m-index). If that is not the case the equation should be ignored. The same rule applies for the expressions for the spatial advection (below) and the magnetic field (below). For the electric field we have:

$$\mathcal{E}_{\ell+1}^m + = E_x \frac{\ell + 1 - m}{2\ell + 1} G_\ell^m, \tag{A.1}$$

$$\mathcal{E}_{\ell-1}^m + = E_x \frac{\ell + m}{2\ell + 1} H_\ell^m, \tag{A.2}$$

$$\mathcal{E}_{\ell+1}^0 + = -\Re\left[(E_y + iE_z) \frac{\ell(\ell + 1)}{2\ell + 1} G_\ell^1\right], \tag{A.3}$$

$$\mathcal{E}_{\ell-1}^0 + = \Re\left[(E_y + iE_z) \frac{\ell(\ell + 1)}{2\ell + 1} H_\ell^1\right], \tag{A.4}$$

$$\mathcal{E}_{\ell+1}^{m+1} + = \frac{(E_y - iE_z)}{2} \frac{1}{2\ell + 1} G_\ell^m, \tag{A.5}$$

$$\mathcal{E}_{\ell+1}^{m-1} + = -\frac{(E_y + iE_z)}{2} \frac{(\ell - m + 2)(\ell - m + 1)}{2\ell + 1} G_\ell^m, \quad m \geqslant 2, \tag{A.6}$$

$$\mathcal{E}_{\ell-1}^{m+1} + = -\frac{(E_y - iE_z)}{2} \frac{1}{2\ell + 1} H_\ell^m, \tag{A.7}$$

$$\mathcal{E}_{\ell-1}^{m-1} + = \frac{(E_y + iE_z)}{2} \frac{(\ell + m - 1)(\ell + m)}{2\ell + 1} H_\ell^m, \quad m \geqslant 2, \tag{A.8}$$

where "+=" stands for the addition-assignment operator: $a += b \Leftrightarrow a = a + b$.

For the spatial advection $\mathcal{A}_\ell^m = \mathcal{A}_{\ell,x}^m + \mathcal{A}_{\ell,y}^m + \mathcal{A}_{\ell,z}^m$ we need to calculate $\partial_x f_\ell^m, \partial_y f_\ell^m$ and $\partial_z f_\ell^m$. We have:

$$\mathcal{A}_{\ell+1}^m + = -\left(\frac{\ell - m + 1}{2\ell + 1}\right) v \partial_x f_\ell^m, \tag{A.9}$$

$$\mathcal{A}_{\ell-1}^m + = -\left(\frac{\ell + m}{2\ell + 1}\right) v \partial_x f_\ell^m, \tag{A.10}$$

$$\mathcal{A}_{\ell+1}^0 + = \Re\left[v \frac{\ell(\ell + 1)}{2\ell + 1}(\partial_y + i\partial_z)f_\ell^1\right], \tag{A.11}$$

$$\mathcal{A}_{\ell-1}^0 + = -\Re\left[v \frac{\ell(\ell + 1)}{2\ell + 1}(\partial_y + i\partial_z)f_\ell^1\right], \tag{A.12}$$

$$\mathcal{A}_{\ell+1}^{m+1} + = -\frac{v}{2}\frac{1}{2\ell + 1}(\partial_y - i\partial_z)f_\ell^m, \tag{A.13}$$

$$\mathcal{A}_{\ell+1}^{m-1} + = \frac{v}{2}\frac{(\ell - m + 2)(\ell - m + 1)}{2\ell + 1}(\partial_y + i\partial_z)f_\ell^m, \quad m \geqslant 2, \tag{A.14}$$

$$\mathcal{A}_{\ell-1}^{m+1} + = \frac{v}{2}\frac{1}{2\ell + 1}(\partial_y - i\partial_z)f_\ell^m, \tag{A.15}$$

$$\mathcal{A}_{\ell-1}^{m-1} + = -\frac{v}{2}\frac{(\ell + m - 1)(\ell + m)}{2\ell + 1}(\partial_y + i\partial_z)f_\ell^m, \quad m \geqslant 2. \tag{A.16}$$

For the magnetic field $\mathcal{B}_\ell^m = \mathcal{B}_{\ell,x}^m + \mathcal{B}_{\ell,y}^m + \mathcal{B}_{\ell,z}^m$ only algebraic operations are required:

$$\mathcal{B}_\ell^m + = -im \times B_x f_\ell^m, \tag{A.17}$$

$$\Re[\mathcal{B}_\ell^0] + = \Re\left[\ell(\ell + 1) \times (B_z - iB_y)f_\ell^1\right], \tag{A.18}$$

$$\mathcal{B}_\ell^{m+1} + = -\frac{1}{2} \times (B_z + iB_y)f_\ell^m, \tag{A.19}$$

$$\mathcal{B}_\ell^{m-1} + = \frac{(\ell - m + 1)(\ell + m)}{2} \times (B_z - iB_y)f_\ell^m, \quad m \geqslant 2. \tag{A.20}$$

References

[1] F. Alouani-Bibi, M.M. Shoucri, J.P. Matte, Different Fokker–Planck approaches to simulate electron transport in plasmas, Comput. Phys. Commun. 164 (1-3) (2004) 60–66. <http://www.sciencedirect.com/science/article/B6TJ5-4CXMXY5-B/2/beddacc6553646400a175c8ca2c6e436>.

[2] H. Azechi, K. Mima, Y. Fujimoto, S. Fujioka, H. Homma, M. Isobe, A. Iwamoto, T. Jitsuno, T. Johzaki, R. Kodama, M. Koga, K. Kondo, J. Kawanaka, T. Mito, N. Miyanaga, O. Motojima, M. Murakami, H. Nagatomo, K. Nagai, M. Nakai, H. Nakamura, T. Nakamura, T. Nakazato, Y. Nakao, K. Nishihara, H. Nishimura, T. Norimatsu, T. Ozaki, H. Sakagami, Y. Sakawa, N. Sarukura, K. Shigemori, T. Shimizu, H. Shiraga, A. Sunahara, T. Taguchi, K. Tanaka, K. Tsubakimoto, Plasma physics and laser development for the fast-ignition realization experiment (firex) project, Nucl. Fusion 49 (10) (2009) 104024 (<http://stacks.iop.org/0029-5515/49/i=10/a=104024>).

[3] A.R. Bell, Nonspitzer heat flow in a steadily ablating laser produced plasma, Phys. Fluids 28 (6) (1985) 2007–2014.

[4] A.R. Bell, R.G. Evans, D.J. Nicholas, Elecron energy transport in steep temperature gradients in laser-produced plasmas, Phys. Rev. Lett. 46 (4) (1981) 243–246.

[5] A.R. Bell, A.P.L. Robinson, M. Sherlock, R.J. Kingham, W. Rozmus, Fast electron transport in laser-produced plasmas and the Kalos code for solution of the Vlasov–Fokker–Planck equation, Plasma Phys. Controlled Fusion 48 (3) (2006) R37–R57.

[6] A.R. Bell, M. Tzoufras, Electron transport and shock ignition, Plasma Phys. Controlled Fusion 53 (4) (2011) 045010. <http://stacks.iop.org/0741-3335/53/i=4/a=045010>.

[7] R. Betti, C.D. Zhou, K.S. Anderson, L.J. Perkins, W. Theobald, A.A. Solodov, Shock ignition of thermonuclear fuel with high areal density, Phys. Rev. Lett. 98 (15) (2007) 155001.

[8] C.K. Birdsall, A.B. Langdon, Plasma Physics via Computer Simulation, Taylor and Francis Group, 270 Madison Avenue, New York, NY, 2005. 10016.

[9] A.V. Bobylev, V.A. Chuyanov, On the numerical solution of landau's kinetic equation, USSR Comput. Math. Phys. 16 (2) (1976) 121–130. <http://www.sciencedirect.com/science/article/B75BX-4903GCR-N8/2/a323513245b9ec988f7b0e9c83adf2c7>.

[10] S.I. Braginskii, Rev. Plasma Phys., vol. 1, Cnsultants Bureau, New York, 1965.

[11] S. Chandrasekhar, Stochastic problems in physics and astronomy, Rev. Mod. Phys. 15 (1) (1943) 1–89.

[12] C.Z. Cheng, G. Knorr, The integration of the Vlasov equation in configuration space, J. Comput. Phys. 22 (3) (1976) 330–351. <http://www.sciencedirect.com/science/article/B6WHY-4DD1NWC-J6/2/59050994c101f0d4c1bd82d45b253cf2>.

[13] B. Chrisman, Y. Sentoku, A.J. Kemp, Physics of plasmas; intensity scaling of hot electron energy coupling in cone-guided fast ignition, Phys. Plasmas 15 (5) (2008) 056309–056309-8.

[14] B.I. Cohen, A.J. Kemp, L. Divol, Simulation of laser-plasma interactions and fast-electron transport in inhomogeneous plasma, J. Comput. Phys. 229 (12) (2010) 4591–4612. <http://www.sciencedirect.com/science/article/B6WHY-4YMK1TF-1/2/62cb90e35406276a50c5ee2716db8e1d>.

[15] R.S. Cohen, L. Spitzer, P.M. Routly, The electrical conductivity of an ionized gas, Phys. Rev. 80 (2) (1950) 230–238.

[16] A. Dolinsky, Numerical integration of kinetic equations, Phys. Fluids 8 (3) (1965) 436–443. <http://link.aip.org/link/?PFL/8/436/1>.

[17] R. Duclous, B. Dubroca, F. Filbet, V. Tikhonchuk, High order resolution of the Maxwell–Fokker–Planck–Landau model intended for icf applications, J. Comput. Phys. 228 (14) (2009) 5072–5100.

[18] R. Duclous, J.-P. Morreeuw, V. Tikhonchuk, B. Dubroca, Reduced multi-scale kinetic models for the relativistic electron transport in solid targets: effects related to secondary electrons, Laser Particle Beams 28 (01) (2010) 165–177.

[19] M. Dunne, A high-power laser fusion facility for europe, Nat. Phys. 2 (1) (2006) 2–5.

[20] J. Huba, NRL Plasma Formulary, Naval Research Laboratory, Washington, DC 20375, 2009.

[21] T.W. Johnston, Cartesian tensor scalar product and spherical harmonic expansions in boltzmann's equation, Phys. Rev. 120 (4) (1960) 1103–1111.

[22] R.J. Kingham, A.R. Bell, An implicit Vlasov–Fokker–Planck code to model non-local electron transport in 2-d with magnetic fields, J. Comput. Phys. 194 (1) (2004) 1–34.

[23] R. Kodama, P.A. Norreys, K. Mima, A.E. Dangor, R.G. Evans, H. Fujita, Y. Kitagawa, K. Krushelnick, T. Miyakoshi, N. Miyanaga, T. Norimatsu, S.J. Rose, T. Shozaki, K. Shigemori, A. Sunahara, M. Tampo, K.A. Tanaka, Y. Toyama, T. Yamanaka, M. Zepf, Fast heating of ultrahigh-density plasma as a step towards laser fusion ignition, Nature 412 (6849) (2001) 798–802. <http://dx.doi.org/10.1038/35090525>.
[24] R. Kodama, Y. Sentoku, Z.L. Chen, G.R. Kumar, S.P. Hatchett, Y. Toyama, T.E. Cowan, R.R. Freeman, J. Fuchs, Y. Izawa, M.H. Key, Y. Kitagawa, K. Kondo, T. Matsuoka, H. Nakamura, M. Nakatsutsumi, P.A. Norreys, T. Norimatsu, R.A. Snavely, R.B. Stephens, M. Tampo, K.A. Tanaka, T. Yabuuchi, Plasma devices to guide and collimate a high density of mev electrons, Nature 432 (7020) (2004) 1005–1008. <http://dx.doi.org/10.1038/nature03133>.
[25] R. Kodama, H. Shiraga, K. Shigemori, Y. Toyama, S. Fujioka, H. Azechi, H. Fujita, H. Habara, T. Hall, Y. Izawa, T. Jitsuno, Y. Kitagawa, K.M. Krushelnick, K.L. Lancaster, K. Mima, K. Nagai, M. Nakai, H. Nishimura, T. Norimatsu, P.A. Norreys, S. Sakabe, K.A. Tanaka, A. Youssef, M. Zepf, T. Yamanaka, Nuclear fusion: fast heating scalable to laser fusion ignition, Nature 418 (6901) (2002) 933–934. <http://dx.doi.org/10.1038/418933a>.
[26] A.B. Langdon, Electron Fokker–Planck transport equation, in: Proceedings of the CECAM Workshop on The Flux Limiter and Heat Flow Instabilities in Laser-Fusion Plasmas, 1982.
[27] R. Lee, M. Lampe, Electromagnetic instabilities, filamentation, and focusing of relativistic electron beams, Phys. Rev. Lett. 31 (23) (1973) 1390–1393.
[28] J.D. Lindl, Inertial Confinement Fusion, Springer-Verlag, New York, 1998.
[29] J.F. Luciani, P. Mora, J. Virmont, Nonlocal heat transport due to steep temperature gradients, Phys. Rev. Lett. 51 (18) (1983) 1664–1667.
[30] W.M. MacDonald, M.N. Rosenbluth, W. Chuck, Relaxation of a system of particles with coulomb interactions, Phys. Rev. 107 (2) (1957) 350–353.
[31] J.P. Matte, J. Virmont, Electron heat transport down steep temperature gradients, Phys. Rev. Lett. 49 (26) (1982) 1936–1939.
[32] D.R. Nicholson, Introduction to Plasma Theory, Wiley, New York, 1983.
[33] P.A. Norreys, R. Allott, R.J. Clarke, J. Collier, D. Neely, S.J. Rose, M. Zepf, M. Santala, A.R. Bell, K. Krushelnick, A.E. Dangor, N.C. Woolsey, R.G. Evans, H. Habara, T.R.K. Norimatsu, Experimental studies of the advanced fast ignitor scheme, Phys. Plasmas 7 (9) (2000) 3721–3726.
[34] F. Peano, M. Marti, L.O. Silva, G. Coppa, Statistical kinetic treatment of relativistic binary collisions, Phys. Rev. E 79 (2) (2009) 025701.
[35] L.J. Perkins, R. Betti, K.N. LaFortune, W.H. Williams, Shock ignition: a new approach to high gain inertial confinement fusion on the national ignition facility, Phys. Rev. Lett. 103 (4) (2009) 045004.
[36] B. Reville, Private Communication, 2011.
[37] X. Ribeyre, M. Lafon, G. Schurtz, M. Olazabal-Loumé, J. Breil, S. Galera, S. Weber, Shock ignition: modelling and target design robustness, Plasma Phys. Controlled Fusion 51 (12) (2009) 124030. <http://stacks.iop.org/0741-3335/51/i=12/a=124030>.
[38] M.N. Rosenbluth, W.M. MacDonald, D.L. Judd, Fokker–Planck equation for an inverse-square force, Phys. Rev. 107 (1) (1957) 1–6.
[39] Y. Sentoku, A.J. Kemp, Numerical methods for particle simulations at extreme densities and temperatures: weighted particles, relativistic collisions and reduced currents, J. Comput. Phys. 227 (14) (2008) 6846–6861. <http://www.sciencedirect.com/science/article/B6WHY-4S8TBBW-1/2/019c3cb20e9e302d570e59f23997bef6>.
[41] M. Sherlock, Universal scaling of the electron distribution function in one-dimensional simulations of relativistic laser-plasma interactions, Phys. Plasmas 16 (10) (2009) 103101. <http://link.aip.org/link/?PHP/16/103101/1>.
[42] I.P. Shkarofsky, T.W. Johnston, T.W. Bachynski, The Particle Kinetics of Plasmas, Addison-Wesley, Reading, MA, 1966.
[43] I.P. Shkarofsky, M.M. Shoucri, V. Fuchs, Numerical solution of the Fokker–Planck equation with a dc electric field, Comput. Phys. Commun. 71 (3) (1992) 269–284. <http://www.sciencedirect.com/science/article/B6TJ5-46G8CJF-8K/2/2397da6102188e0de2859637cf244c0d>.
[44] L. Spitzer, R. Härm, Transport phenomena in a completely ionized gas, Phys. Rev. 89 (5) (1953) 977–981.
[45] M. Tabak, J. Hammer, M.E. Glinsky, W.L. Kruer, S.C. Wilks, J. Woodworth, E.M. Campbell, M.D. Perry, R.J. Mason, Ignition and high gain with ultrapowerful lasers, Phys. Plasmas 1 (5) (1994) 1626–1634. <http://link.aip.org/link/?PHP/1/1626/1>.
[46] A.G.R. Thomas, R.J. Kingham, C.P. Ridgers, Rapid self-magnetization of laser speckles in plasmas by nonlinear anisotropic instability, New J. Phys. 11 (3) (2009) 033001. <http://stacks.iop.org/1367-2630/11/i=3/a=033001>.
[47] M. Tzoufras, C. Ren, F.S. Tsung, J.W. Tonge, W.B. Mori, M. Fiore, R.A. Fonseca, L.O. Silva, Space-charge effects in the current-filamentation or weibel instability, Phys. Rev. Lett. 96 (10) (2006) 105002.
[48] E.S. Weibel, Spontaneously growing transverse waves in a plasma due to an anisotropic velocity distribution, Phys. Rev. Lett. 2 (3) (1959) 83–84.